Jeoloji Mühendisliği Dergisi / *Journal of Geological Engineering*
49 (2025) 43-80
DOI 10.24232/jmd.1701986

Araştırma Makalesi / *Research Article*

Mineral Reaction Kinetics During CO_2 Sequestration into Paleozoic Metamorphic Rocks

Paleozoyik Yaşlı Metamorfik Kayaçlara CO_2 Tutulumu Sırasında Mineral Tepkime Kinetiği

Hakki AYDIN[1*], Selçuk EROL[2], Serhat AKIN[3]

[1] *Zorlu Energy Group, Sarayköy, Denizli, Türkiye*

[2] *Izmir Institute of Technology, Izmir, Türkiye*

[3] *Middle East Technical University, Ankara, Türkiye*

Geliş *(Received)*: 19/05/2025 / Düzeltme *(Revised)*: 23/07/2025 / Kabul *(Accepted)*: 04/08/2025

ABSTRACT

Carbon dioxide (CO_2) sequestration into geological formations is one of the most reliable methods for mitigating CO_2 emissions. Geothermal reservoirs are excellent candidates for CO_2 trapping due to considerable fracture pore volume, which provides safe and permanent storage. The stability of the target reservoir rock and caprock is a critical topic during long-term CO_2 sequestration. This study examines the geochemical changes resulting from reactions between geothermal reservoir rock and CO_2-saturated brine. The ultimate aim is to understand the efficiency of CO_2 sequestration in a metamorphic geothermal reservoir regarding its geochemical impact. The study involves batch experiments on core samples taken from depths of 1900 m and 3000 m in the Kızıldere geothermal reservoir in western Türkiye. We exposed crushed core samples to CO_2-saturated geothermal brine at a temperature of 95 °C and a pressure of 10 bar for 21 days. Experimental changes in the concentrations of major elements (Mg^{2+}, Ca^{2+}, Al^{3+}, Fe^{2+}, SiO_2, and Cl^-) were simulated using PHREEQC software. Kinetic rates and activation energy were utilized as tuning parameters to align simulation outcomes with experimental observations. The behavior of Mg^{2+} and Ca^{2+} exhibited an increasing trend, while SiO_2, Al^{3+}, and Fe^{2+} demonstrated a decreasing trend. Consequently, the interaction between CO_2-saturated brine and reservoir rock resulted in the precipitation of K-feldspar and kaolinite minerals, whereas other minerals, such as biotite, quartz, magnesite, and siderite, exhibited slight dissolution. The mineral assemblage remained consistent, while the abundance of the minerals exhibited slight variations. The study indicates that a high concentration of cations may facilitate the trapping of CO_2 within metamorphic rocks. Furthermore, solubility trapping was determined to be more significant than mineral trapping in the batch experiments.

Keywords: Carbon dioxide sequestration, mineral alteration, geothermal energy

ÖZ

Jeolojik formasyonlara karbondioksit (CO_2) tutulumu, CO_2 emisyonlarını azaltmak için en güvenilir yöntemlerden biridir. Jeotermal rezervuarlar, geniş kırık-gözenek hacimleri sayesinde CO_2 tutumu için güvenli ve kalıcı depolama fırsatları sunan mükemmel adaylardır. Hedef rezervuar kayacı ve örtü kayacın uzun dönem CO_2 enjeksiyonu süresince kararlılığı ise kritik bir konudur. Bu çalışma, jeotermal rezervuar kayacı ile CO_2 doygunluğundaki akışkan arasındaki reaksiyonlar sonucu oluşan jeokimyasal değişimleri incelemektedir. Nihai amaç, metamorfik bir jeotermal rezervuarda CO_2 tutumunun jeokimyasal etkiler açısından etkinliğini ortaya koymaktır. Çalışma

Sorumlu yazar / *Corresponding author:* hakki_aydin1990@hotmail.com

kapsamında, Türkiye'nin Batısında yer alan Kızıldere jeotermal rezervuarında 1900 m ve 3000 m derinliklerden alınan karot numuneleriyle kesikli (batch) deneyler gerçekleştirilmiştir. Ufaltılmış karot örnekleri, 95 °C sıcaklık ve 10 bar basınçta CO_2 doygunluğundaki jeotermal akışkana 21 gün süreyle maruz bırakılmıştır. Mg^{2+}, Ca^{2+}, Al^{3+}, Fe^{2+}, SiO_2 ve Cl^- gibi temel element konsantrasyonlarındaki deneysel değişimler PHREEQC yazılımı kullanılarak modellenmiştir. Simülasyon çıktılarının deneysel gözlemlerle uyumlu olması için kinetik hızlar ve aktivasyon enerjisi ayar parametreleri olarak kullanılmıştır. Mg^{2+} ve Ca^{2+} konsantrasyonları artış eğilimi gösterirken; SiO_2, Al^{3+} ve Fe^{2+} azalma eğilimi göstermiştir. Bu durum, CO_2 doygun akışkan ile rezervuar kayacı arasındaki etkileşim sonucunda K-feldispat ve kaolinit minerallerinin çökelmesine yol açmış; biyotit, kuvars, manyezit ve siderit gibi diğer minerallerde ise hafif çözünme meydana gelmiştir. Mineral topluluğu genel olarak sabit kalmış, ancak minerallerin bollukları küçük değişiklikler göstermiştir. Çalışma, yüksek katyon konsantrasyonlarının metamorfik kayaçlar içerisinde CO_2 tutumunu kolaylaştırabileceğini ortaya koymuştur. Ayrıca, gerçekleştirilen kesikli deneylerinde çözelti fazında CO_2 tutulumunun mineral tutulumuna kıyasla daha baskın olduğu belirlenmiştir.

Anahtar Kelimeler: *Karbondioksit tutulumu, mineral alterasyonu, jeotermal enerji*

INTRODUCTION

The terms "global warming" and "climate change" denote long-term alterations in atmospheric conditions, including humidity, temperature, and precipitation patterns, attributed to elevated anthropogenic CO_2 levels and other greenhouse gas emissions (Thuiller, 2007; Taylor et al. 2013). Researchers are actively exploring strategies to diminish CO_2 emissions and manage climate change effectively. The sequestration of CO_2 into geological formations represents one of the most dependable and secure techniques for alleviating gas emissions that contribute to global warming (Bachu, 2000; Shukla et al., 2010; Andre et al., 2012; Jin et al., 2016). Deep geothermal reservoirs are recognized as promising geological formations for the long-term sequestration of carbon dioxide (CO_2). Capturing the CO_2 emissions from geothermal sites and reinjecting them into the original geothermal reservoir constitutes an additional method to mitigate emissions. In the CarbFix method (Aradottir et al., 2012), the geothermal effluent is combined with the captured non-condensable gas (NCG) and cold pond water. The resulting CO_2-saturated brine is then injected into the same geothermal reservoir (Clark et al., 2020; Galeczka et al., 2022). Throughout this process, the injected CO_2 is first captured via solubility trapping. This CO_2 can subsequently convert into bicarbonate and carbonic acid when it interacts with the formation brine. This interaction triggers complex chemical reactions that allow CO_2 to be sequestered in a secondary mineral phase as carbonate, depending on the prevailing thermodynamic conditions and the presence of primary mineral phases (Matter et al., 2016; Přikryl et al., 2018). Primary minerals crystallize directly from magma and are mainly found in igneous rocks, while secondary minerals form through the alteration or weathering of primary minerals (Berndsen et al., 2024). Following the success of the CarbFix projects, the insights gained are being applied to other geothermal sites across Europe, such as those in Türkiye and Italy, under the Geothermal Emission Control H2020 project (GECO, 2020; GECO, 2023).

Geological CO_2 storage capacity depends on the volume, as well as the chemical and mineralogical composition of the formation brine and reservoir rock, respectively. CO_2 sequestration can be achieved through the following mechanisms:

- CO_2 dissolution in formation water, which is called solubility trapping
- Mineral trapping as a result of interactions between CO_2-saturated water and the rock
- CO_2 accumulation at the top of geological strata called structural trapping
- Hydrodynamic trapping occurs when the density of CO_2 is near that of the formation brine (Zhang & Song, 2019)
- Capillary trapping involves CO_2 injection into a saline aquifer (drainage process), and brine is passively re-imbibed into the pore space (imbibition process) (Teng et al., 2022)

Long-term structural trapping, capillary trapping, and hydrodynamic trapping may pose risks, including gas leakage through conductive faults, cementing failure, and surface deformation. Therefore, mineral and solubility trapping are considered the most reliable and safe mechanisms to mitigate CO_2 emissions. Geothermal reservoirs are suitable candidates for this purpose due to their large brine volume. However, it is important to note that CO_2 solubility decreases with increasing salinity (Duan and Suni, 2003; Duan et al., 2006). To minimize risks before field-scale CO_2 injections, experimental and simulation-based studies are typically conducted to delineate possible effects on well integrity, reservoir rock, and caprock.

Interactions between brine and rock can be analyzed through the implementation of batch and core-flood experiments. Reactive minerals, as well as both primary and secondary minerals, can be acquired through laboratory tests. However, it is important to note that laboratory experiments may be insufficient to fully account for the intricate reaction pathways present in natural systems (Hellevang et al., 2013). Furthermore, numerical simulations are capable of forecasting reactive-transport processes in complex natural systems over extensive timeframes, potentially spanning thousands of years. These numerical simulations necessitate the availability of thermodynamic and kinetic data to ensure the accuracy of these predictions. Barlas et al. (2024) simulated CO_2 injection into the Kızıldere geothermal field and reported that the results of the CO_2-charged brine injection showed that approximately 20% of the injected CO_2 circulated in the reservoir, ensuring reduced CO_2 emissions. Hydrothermal alteration constitutes a complex process characterized by a range of chemical, textural, and mineralogical transformations that indicate fluid circulation within geothermal formations. This process occurs during the stages of recharge, upward flow, and burial metamorphism. Types of alteration may vary based on critical parameters such as deposit type, environmental temperature, pressure, fluid-to-rock ratio, and fluid content. The extent of the alteration zone may range from a few centimeters to several kilometers. There are two primary divisions of alteration: hypogene alteration and supergene alteration. An increase in temperature typically induces hypogene alteration, whereas supergene alteration occurs because of meteoric water reactions in low-temperature environments (Brimhall and Ghiorso, 1983). Notable mineral alterations include potassic alteration, phyllic alteration, propylitic alteration, argillic alteration, silicification, carbonization, greisenization, and hematitization (Wallace & Maher, 2019; Seki, 1973; Parry et al., 2002; Di Tommaso & Rubinstein, 2007). Potassic alteration occurs by replacing plagioclase and mafic silicates at temperatures between 450 and 600 °C. K-silicate is characterized by K-feldspar, biotite, minor quartz, and chlorite (Battles and Barton, 1995). Propylitic alteration occurs through the addition of H_2O, CO_2, and local S, without appreciable H^+

metamorphism. Chlorite and epidote primarily exist alongside lesser amounts of calcite, albite, and zoisite in a propylitic alteration environment (Binglin et al., 2014). Propylitic alteration is found at low to intermediate temperatures (200-350 °C) and low fluid-rock ratios. The destabilization of feldspars results in sericitic alteration through hydrolysis in the presence of K, S, and OH, forming quartz, chlorite, pyrite, and sericite (Meunier & Velde, 1976). This process involves leaching out of Mg, Fe, Na, Ti, and K. Argillic alteration is categorized into intermediate and advanced argillic depending on the intensity of the clay mineral. Intermediate argillic alteration is characterized by the formation of smectite and kaolinite groups at temperatures below 250 °C (Hikov, 2004). Silicification involves forming new quartz or amorphous silica minerals as a result of isochemical hydrolysis reactions in the local presence of Si. Quartz precipitation occurs in fractures where hydrothermal fluids flow. High-level epithermal precious metal ore deposits influence silicification (Kumar & Ghassemi, 2005). Carbonatization refers to the formation of carbonate minerals such as dolomite, calcite, siderite, and magnesite during rock alteration. Mineral carbonation requires metallic cations such as Mg^{2+}, Ca^{2+}, and Fe^{2+}. Greisenization represents the alteration of muscovite, quartz, and lesser fluorite (Witt, 1988). It is a post-magmatic alteration that changes the composition of granites through several sequential stages. It is a metasomatic process related to high silica leucocratic granitoid (Stemprok, 1987). A summary of alteration types and their mineral compositions is shown in Table 1. Secondary minerals observed in western Türkiye are presented in Table 2.

Table 1. Diagnostic minerals in hydrothermally-altered volcanogenic massive sulfide deposits at various metamorphic grades (Alt et al., 2012).

Çizelge 1. Farklı metamorfizma derecelerine uğramış hidrotermal olarak altere olmuş volkanik kökenli masif sülfit yataklarındaki tanısal mineraller (Alt vd., 2012).

Alteration type	**Diagnostic minerals: unmetamorphosed deposits**	**Diagnostic minerals: greenschist facies**	**Diagnostic minerals: granulite facies**
Advanced argillic	Kaolinite, alunite, opal, smectite	Kaolinite, pyrophyllite, andalusite, corundum, topaz	Sillimanite, kyanite, quartz
Argillic	Sericite, illite, smectite, pyrophyllite, opal	Sericite, illite, pyrophyllite	Sillimanite, kyanite, quartz, biotite, cordierite, garnet
Sericitic	Sericite, illite, pyrophyllite	Sericite, illite, quartz	Biotite, K-feldspar, sillimanite, kyanite, quartz, cordierite, garnet
Chloritic	Chlorite, quartz, sericite	Chlorite, quartz, sericite	Cordierite, orthopyroxene, orthoamphibole, phlogopite, sillimanite, kyanite
Carbonate propylitic	Carbonate (Fe, Mg), epidote, chlorite, sericite, feldspar	Carbonate (Fe, Mg), epidote, chlorite, sericite, feldspar	Carbonate, garnet, epidote, hornblende, diopside, orthopyroxene

Table 2. Secondary minerals observed as a result of water-rock interaction in western Türkiye.
Çizelge 2. Batı Türkiye'de su–kayaç etkileşimleriyle oluşan ikincil mineral toplulukları.

Field ID	Water type	Reservoir rock type	Hydrothermal Alteration	References
Aydın-Salavatlı Geothermal Field	Na-HCO_3	Menderes metamorphic reservoir rock (calc-schist, mica-schist, quartzite, gneiss, marble)	Kaolinite, illite, montmorillonite, calcite, pyrite, dolomite, and hydro biotite	Karamanderesi & Helvaci, 2003
Alaşehir Geothermal Field	Na-HCO_3	Menderes metamorphic reservoir rock (calc-schist, mica-schist, quartzite, marble)	Chloritization, sericitization, silicification, carbonification	İlhan & Kabak, 2018
Kızıldere Geothermal Field	Na-HCO_3SO_4	Menderes metamorphic reservoir rock (calc-schist, mica-schist, quartzite, marble)	Phyllic, argillic, silicic, hematized, and carbonatized alteration zones	Özgür, 2010

Geological storage of carbon dioxide is a slow process that may require years. Critical parameters influencing the reaction time include mineral surface area, mineral types, thermodynamic conditions, and CO_2 saturation. Flow-through experiments can take months to years to understand brine-rock interaction due to the limited contact surface area. In contrast, batch experiments have a considerably shorter experimental time due to the high mineral surface area of rock in powder form. Consequently, laboratory test results typically provide some insights into process initiation. In this regard, reactive transport simulations calibrated with experimental results are generally employed to understand the effects of CO_2 reinjection on the reservoir rock and fluid (Ratouis et al., 2021; Ratouis et al., 2022; Erol et al., 2022a). Kinetic reaction rates and mineral surface area significantly influence fluid-rock interaction. Estimating reservoir mineral surface area can be challenging in heterogeneous systems. Therefore, sensitivity analyses are performed to understand its impact on the results. Reaction rates obtained from laboratory tests may differ from those determined in natural field settings (White & Brantley, 2003). Kampman et al. (2014) noted that direct sampling of CO_2-rich fluids is complicated due to CO_2 degassing during sampling. Waldmann et al. (2014) investigated the significance of mineral surface area on CO_2-brine-rock interactions. They studied the effects of specific mineral surface areas, mineral distribution, and whole rock surface areas separately. The study demonstrated that the initial amounts of K-feldspar, hematite, kaolinite, and carbonate control clay mineral precipitation during CO_2 storage in Rotliegend sandstones.

Gaseous impurities can lead to various reactions at different kinetic rates. Pearce et al. (2015) conducted both experimental and simulation studies to investigate the impact of SO_2 on CO_2-brine-rock interactions. The dissolution of SO_2 in water produced sulfuric acid, which intensified the dissolution of

silicates and carbonates. The degree of mineral dissolution varies depending on the rock composition. Their research indicated that high cation concentrations may enhance CO_2 trapping. Wang et al. (2016) investigated CO_2-brine-rock interactions for CO_2 sequestration in deep coal seams through experimental methods. Their experiments utilized powdered rock samples to simulate caprock in a batch system, conducted at 160 °C and 15 MPa. They analyzed changes in mineralogical composition using X-ray diffraction (XRD) and energy dispersive X-ray spectroscopy with scanning electron microscopy (EDX-SEM) techniques.

Batch reactor experiments effectively enhance our understanding of the interactions between CO_2-saturated brine and reservoir rock under actual reservoir conditions. Steel et al. (2018) carried out hydrothermal experiments lasting over six months to investigate the potential for mineral carbonation through brine buffering with calcite. These experiments were subsequently simulated using PHREEQC to assess the equilibrium state. The findings indicated that the buffering effect of calcite was inadequate to promote mineral carbonation. Liu et al. (2012) examined reactive experiments involving CO_2, brine, and caprock, presenting the Eau Claire formation as a case study. A batch experiment was executed at 200 °C and 300 bars. Stable isotope tests indicated the presence of CO_2 in both free and dissolved phases within the caprock. The study noted the precipitation of clay and carbonate minerals alongside the dissolution of feldspars and carbonate minerals. Liu et al. (2018) explored CO_2-brine-rock interactions aimed at CO_2 sequestration in a deep saline aquifer. They conducted experiments using minerals sourced from the upper layer of the Shahejie formation in China. The results revealed significant changes in ion concentrations after 72 hours of reaction time, with notable increases in HCO_3 and Ca^{2+} concentrations.

Water-rock interaction experiments and simulations are critical components of CO_2 sequestration projects. This study investigates CO_2 sequestration in Paleozoic geothermal reservoir rocks. The results of batch experiments, coupled with a modeling approach, are used to understand water-rock interaction during injection of brine containing dissolved CO_2. Geochemical changes in the brine and mineral alterations were measured through analyses of both water and rock. Important parameters, such as mineral surface area, kinetic reaction rate, and activation energy, affecting water-rock interaction were determined by matching experimental results with a modeling approach using PHREEQC.

GEOLOGY OF KIZILDERE GEOTHERMAL SYSTEM

The Kızıldere geothermal field is located at the eastern boundary of the Büyük Menderes graben, one of the most active extensional structures within the western Anatolian graben-horst system. The Kızıldere field developed within an extensional domain play type, where convective and conductive heat flow effectively dominate geothermal activity. Various tectonic movements have influenced Western Anatolia over time. These have led to crustal thinning and the formation of large grabens in the region (Şengör & Yılmaz, 1981).

The stratigraphy of this field comprises Paleozoic metamorphic units of the Menderes Massif, overlain by Pliocene and Quaternary sedimentary rocks. The rock units cropping out near the Kızıldere geothermal field were studied by various researchers (Şimşek, 1984; Sun,

1990; Bozkurt, 2000; Kaymakçı, 2006; Alçiçek et al., 2007; Gürer et al., 2009; Koçyiğit, 2015). There is no consensus about the names and ages of the units in the region, as shown in Figure 1. However, a recent study by Aksu (2019) is based on a definition of formations derived from drilling more than 100 geothermal wells and is more widely used in field operations. The stratigraphy of the study area, from oldest to youngest, comprises the Menderes Massif, the Kızılburun Formation, the Sazak Formation, the Kolankaya Formation, the Tosunlar Formation, and Quaternary alluvial deposits.

The Menderes Massif, first identified and named by Philipson (1918), is the largest tectonic unit in western Anatolia. Bozkurt and Oberhansli (2001) classified the Menderes Massif into two rock groups: core rocks and cover rocks. Core rocks include augen gneiss, metagranite, quartzite, and other high-pressure, high-temperature metamorphic rocks (Şengör et al., 1984). Aksu (2019) described augen gneiss as very coarse-grained, brittle, extensively weathered, and highly fractured in the Kızıldere field outcrops. The cover rocks include low-grade quartzite, schist, and marble. Schist bands in the region include calc-schist, quartz-muscovite-schist, mica-schist, and chlorite-schist. The age of the cover rocks is Mesozoic-Paleozoic (Boray, 1982).

The Kızılburun Formation dates back to the Early Miocene to Early Middle Miocene period (Alçiçek et al., 2007). It overlies the Menderes Massif and can be described as matrix-supported, unsorted, polygenetic boulder-block conglomerates with intercalations of red-brown mudstone and sandstone (Aksu, 2019).

The Sazak Formation conformably overlies the Kızılburun Formation. Its lower section features gray-green marl, brown claystone, and alternating layers of clayey limestone. The middle section is marked by massive limestone beds alternating with sandstones. The upper section comprises clayey limestone and organic-rich calcareous shale facies. The karstic characteristics and brittle rheology of the Sazak Formation make it a highly effective reservoir for the geothermal system in the Kızıldere field. Hot springs and fumeroles are observed in the limestone units of the Sazak Formation in the study area.

The Kolankaya Formation is characterized by laminated marl with occasional intercalations of sandstone and bioclastic limestone. Marl deposits suggest a much deeper, low-energy lacustrine environment with brackish water conditions compared to the Sazak Formation (Alçiçek et al., 2007).

The Tosunlar Formation lies above all older rocks, separated by a regional unconformity. It is composed of yellow-brown, polygenetic, poorly-sorted conglomerates made of pebbles and boulders, with occasional mudstone layers. The formation was deposited as a fault-controlled high-energy debris flow along mountain fronts (Aksu, 2019).

Holocene units comprise loose, poorly-sorted materials including pebbles, sands, and muds from alluvial fan and fluvial deposits. Alluvial fan deposits are located near the basin margins, whereas fluvial alluvium deposits are found in the basin center.

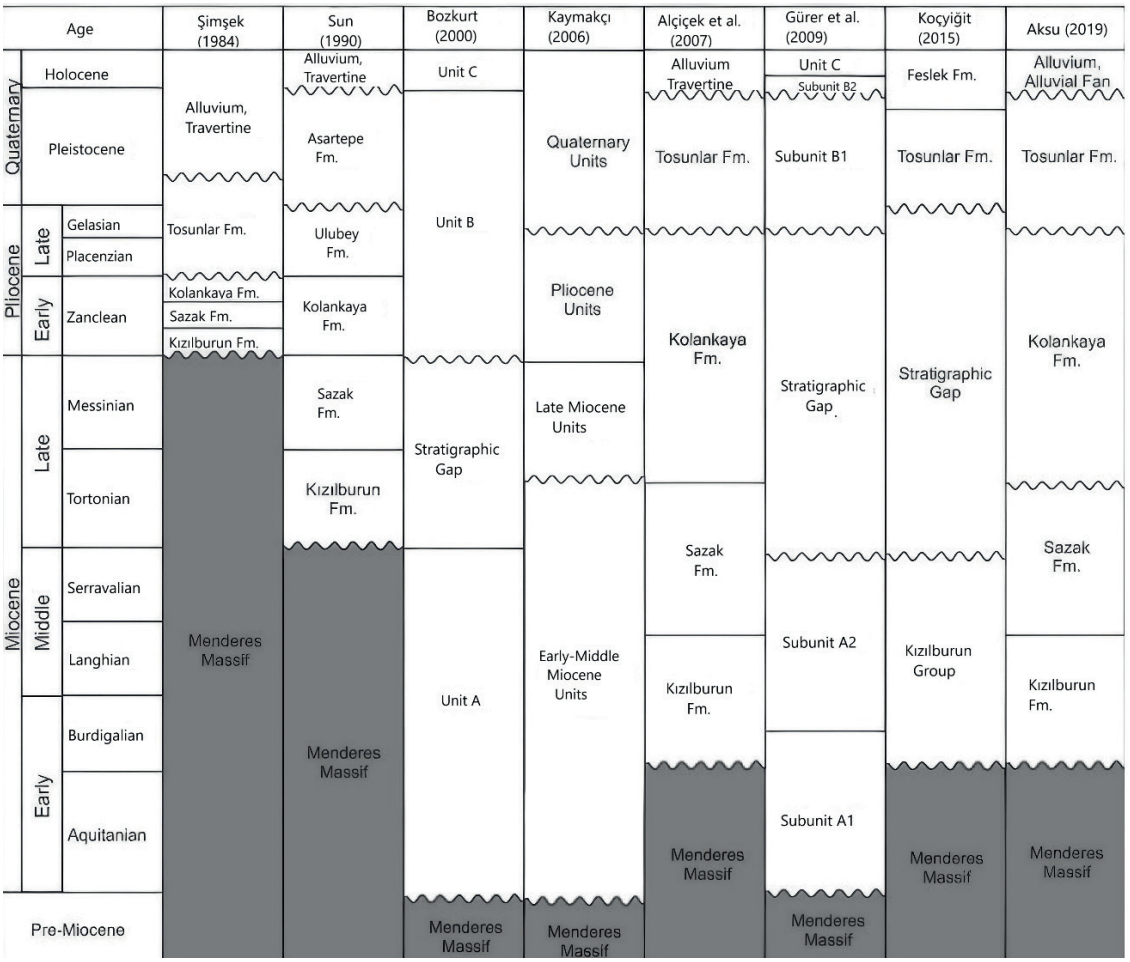

Figure 1. Stratigraphic comparison from previous studies based near Kızıldere geothermal field (adapted from Aksu, 2019).

Şekil 1. Kızıldere jeotermal sahası çevresinde derlenen önceki çalışmaların stratigrafik karşılaştırması (Aksu, 2019'dan revize edilmiştir).

In the Kızıldere geothermal field, there are four main productive reservoir sections arranged by increasing depth: Sazak Formation (Reservoir I), İgdecik Formation (Reservoir II), fractured quartzite-calcschist of the Menderes Metamorphics (Reservoir III), and the deep marble section of the Menderes Metamorphics (Reservoir IV) (Haklıdır et al., 2021). The sections where core samples were collected during the drilling of a geothermal well are shown in Figure 2.

Core sample #1 was retrieved from a depth of 1900 meters, where the reservoir rock is characterized as quartzite with white, dirty white, greenish, dull, transparent, and translucent features. It is extremely hard, with microfractures, containing mica flakes, trace pyrite, infilling silica, and chlorite schist banding. Core sample

#2 was collected from a depth of 3000 m, where the reservoir rock is marble characterized by light to dark grey coloration, mottled, hard to extremely hard, microcrystalline, fractured and microfractured, partly silicified, massive, tight texture, and intercalated with calcschist. It is essential to note that the mineralogical composition of the core samples does not represent the entire reservoir rock, but rather a single point within the highly heterogeneous system.

A geological map of the study area at a scale of 1:25000 is presented in Figure 3. Outcrops of geological units can be observed in the field. Three fault types were identified in the geothermal system: approximately E-W-striking high-angle normal faults, N-S-striking subvertical faults, and an old low-angle detachment fault that likely developed prior to the other faults. Geothermal wells that target intersecting faults at reservoir depths deliver good production results because fractures enhance secondary permeability.

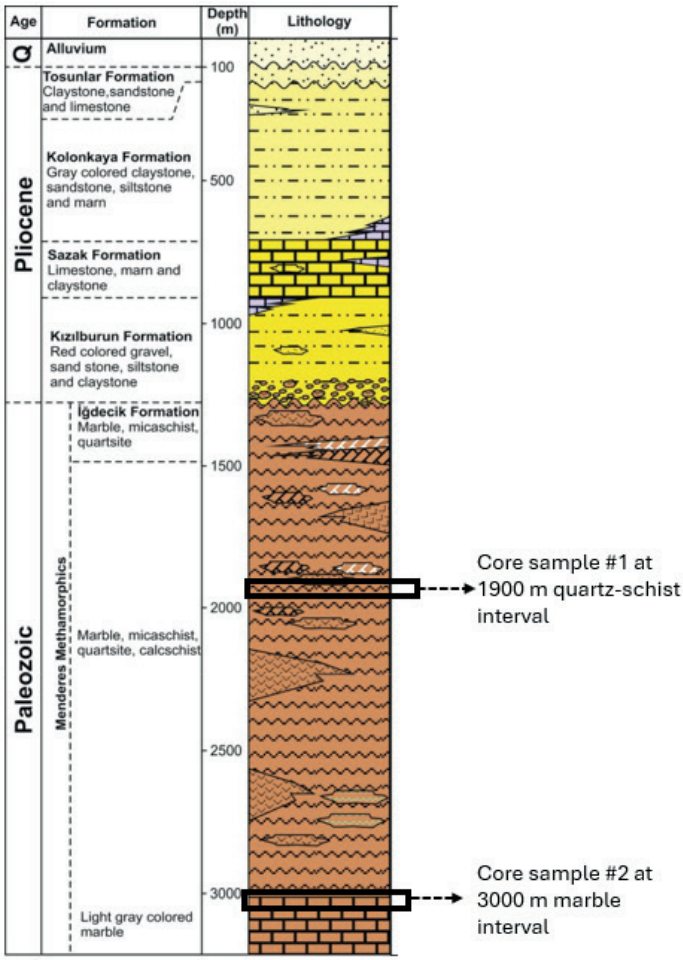

Figure 2. Geological columnar section and depths of core samples from the study area (adapted from Haklıdır et al., 2021)

Şekil 2. Jeolojik sütun kesiti ve karot örneklerinin derinlikleri (Haklıdır vd., 2021'den revize edilmiştir).

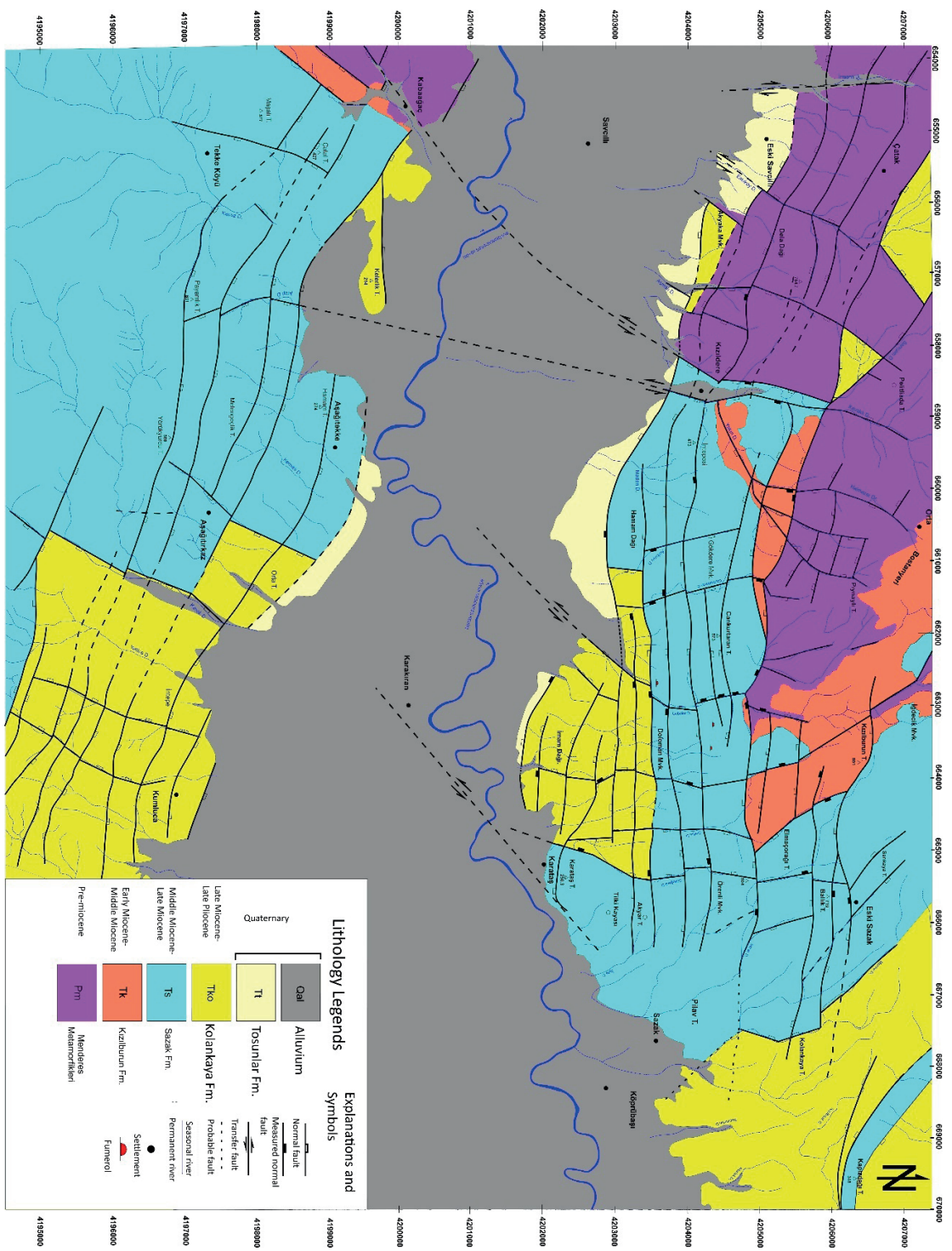

Figure 3. Geological map of the study area (after Aksu, 2019).

Şekil 3. Çalışma alanının jeolojik haritası (Aksu, 2019'dan alınmıştır).

MATERIALS AND METHODS

The workflow for the study is depicted in Figure 4. The study started by collecting actual geothermal brine and NCG (more than 99% CO_2) from geothermal wells. Core samples were taken from depths of 1900 m and 3000 m in the Kızıldere geothermal reservoir in Türkiye (Senturk et al., 2020). The core samples were then crushed and screened into particle sizes. The methodology and the experimental setup process are presented in Aydin and Akin (2023). Each batch experiment was performed twice under the same conditions to ensure consistency and evaluate reproducibility. The results are the averages of these repeated runs. Any variation between duplicates remained within acceptable analytical uncertainty. Rock analysis was performed before and after batch experiments using XRD, EDX-SEM, and a polarized light microscope. XRD analyses of the powdered samples were performed at Pamukkale University Advanced Technology Research and Application Center (PAU-ILTAM) Laboratory using a GNR APD 2000 diffractometer. The instrument features a Cu-Kα cathode tube (wavelength: 1.54 Å) and operates under the following conditions: voltage of 10–60 kV, current of 5–60 mA, scanning speed of 0.1°(2θ/s), and scanning range from 111° to 168° (2θ). Based on the resulting XRD patterns, mineralogical identifications and the relative abundances of minerals (%) were determined. SEM-EDS analyses were conducted at the Advanced Research Techniques Laboratory of Pamukkale University using a Carl Zeiss FESEM Supra 40 VP field emission scanning electron microscope. Backscattered electron (BSE) imaging was used to obtain microstructural data, and semi-quantitative chemical compositions of minerals in the core samples were determined with a Quantax Bruker EDS system. Polarized light microscope measurements were carried out at the Department of Geological Engineering, Pamukkale University, using a Carl Zeiss Primotech polarizing microscope equipped with both transmitted and reflected light illumination.

Additionally, image processing was employed to determine the mineral surface area, a critical parameter for modeling the reaction process. Similarly, geochemical measurements of major elements were conducted before and after the batch experiments. In batch experiments, the PHREEQC code was used to simulate water-rock interaction between CO_2-saturated geothermal brine and rock particles (Parkhurst & Appelo, 2013). The tuning parameters were the activation energy and the kinetic reaction rates of minerals, which were adjusted to match the simulation data with the concentrations of elements obtained from experiments.

The study features batch experiments focused on the interaction between rock powders and CO_2-saturated geothermal brine. An illustration of the experimental setup is depicted in Figure 5. This arrangement includes a reactor with a 12-liter inner volume, geothermal heating, a mixer (shown in Figure 6d), a Sierra-branded gas flow meter (Figure 6a), a high-pressure gas source tube, a two-stage regulator, sampling ports, and a mini separator (Figure 6a). To minimize reactions that could alter the geothermal brine, stainless steel components were employed. Two ¼-inch injection ports (Figure 6b) are positioned at the reactor's top to facilitate the injection of gas and brine. A pressure relief valve ensures safe pressure release in the event of uncontrolled increases within the reactor. The batch reactor includes a mixer with a power rating of 0.75 kW (Figure 6c), a 300-rpm reducer, Teflon packing, and a specialized sealing system, allowing continuous mixing at elevated temperatures and pressures. The system's temperature and pressure

are constantly recorded by a thermocouple and a pressure transmitter located at the bottom of the reactor. Insulation materials and a double-stage gas regulator maintain stable temperature and pressure conditions during experiments. The reactor is heated using the temperature of the geothermal brine from the production line. Brine samples are taken from the sampling port at the bottom of the reactor and routed to a mini separator under atmospheric conditions. Here, the flashed brine sample separates into gas and liquid phases, with brine samples collected from the bottom port of the mini separator. The gas phase is funneled into a steam condenser to remove steam from NCG, while pure and dry CO_2 is quantified using a gas flow meter.

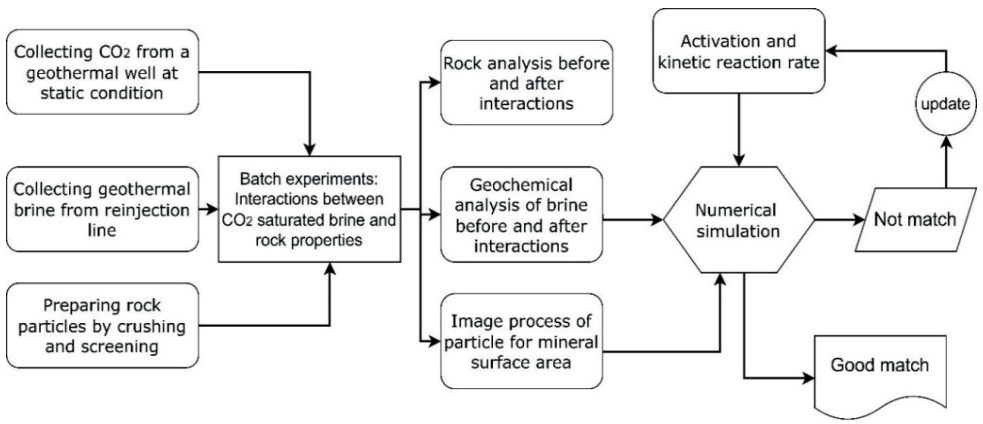

Figure 4. Workflow of the study.
Şekil 4. Çalışmanın iş akışı.

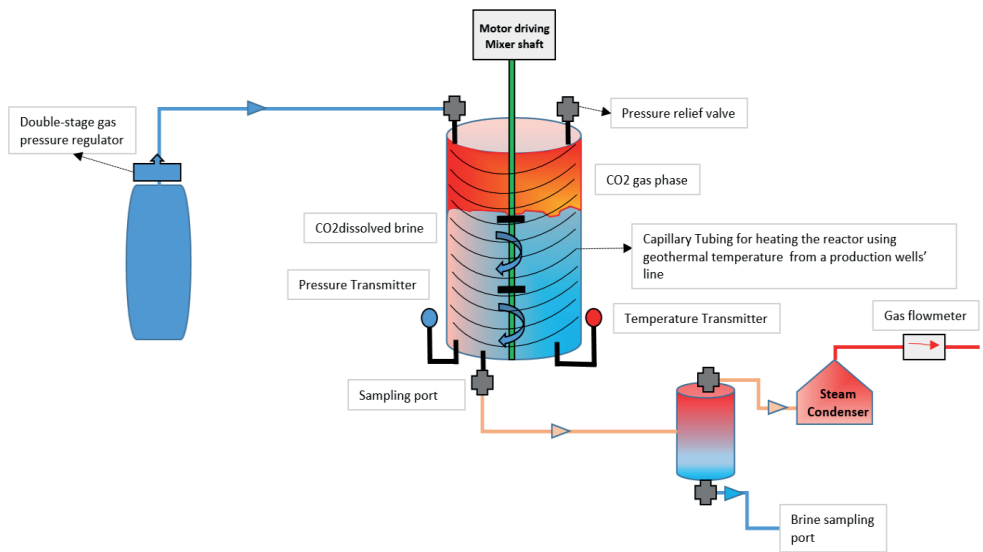

Figure 5. Illustration of the experimental setup.
Şekil 5. Deney düzeneğinin şematik gösterimi.

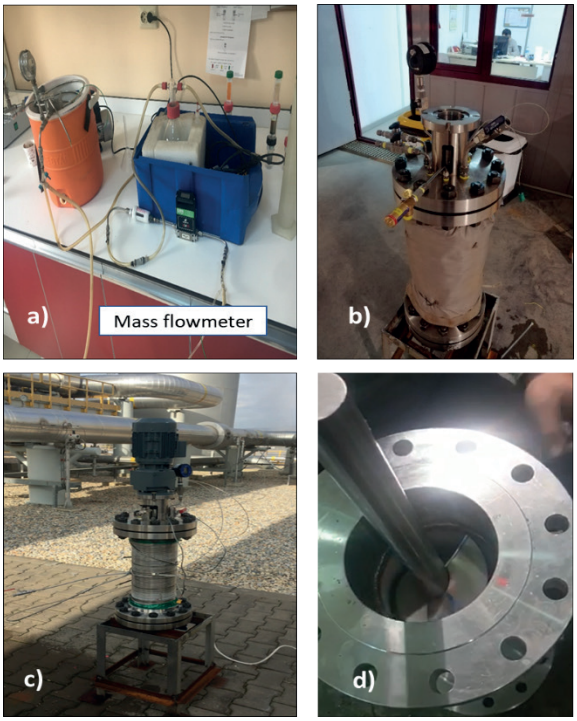

Figure 6. Equipment in the experimental setup; a) mass flowmeter and condenser, b) relief valve, gas and liquid injecting ports, c) reactor with a mixing motor and heating system, and d) mixer and rotor

Şekil 6. Deney düzeneğinde kullanılan ekipmanlar: a) Kütlesel debimetre ve yoğuşturucu.

b) Emniyet vanası, gaz ve sıvı enjeksiyon girişleri c) Karıştırma motoru ve ısıtma sistemi bulunan reactor d) Karıştırıcı ve rotor.

The geothermal brine (9 liters) was gathered from an injection well in the Alaşehir field and introduced into the reactor. CO_2 was likewise sourced from a geothermal well, maintained under static conditions with a pressure of 40 bar at the wellhead (Figure 7). The brine sample was heated using the heat from an actively-producing geothermal well and then routed into capillary tubing that is encircled by the reactor. The reactor was subsequently insulated from the atmosphere with isolating materials. Once temperature stabilization was achieved, CO_2 was supplied to the reactor at constant pressure while the system underwent continuous mixing. This consistent mixing of the fluids within the reactor maximizes the contact surface area between geothermal brine and CO_2 (Figure 8).

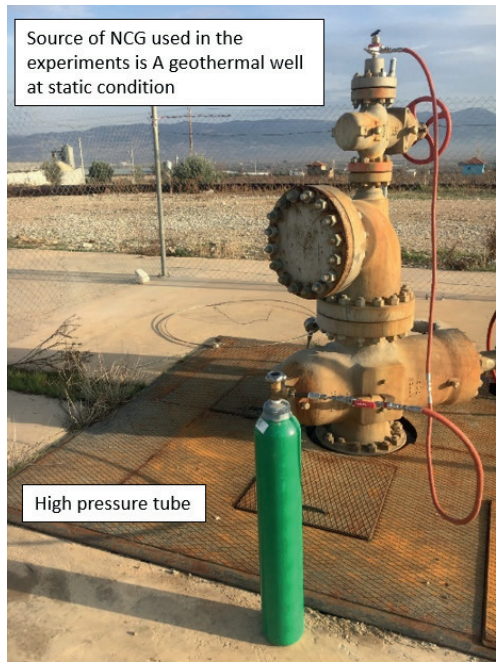

Figure 7. Gas collecting at a well for the experiments.

Şekil 7. Deneylerde kullanılan gaz toplama kuyusu.

The gas content of the NCG is shown in Table 3. As can be seen, CO_2 constitutes more than 99% of the total dry gas volume. The geothermal well has not flowed for over 16 months, and NCG accumulation occurred at the wellhead due to density differences. The geochemical content of the geothermal brine collected from the re-injection line is also presented in Table 4.

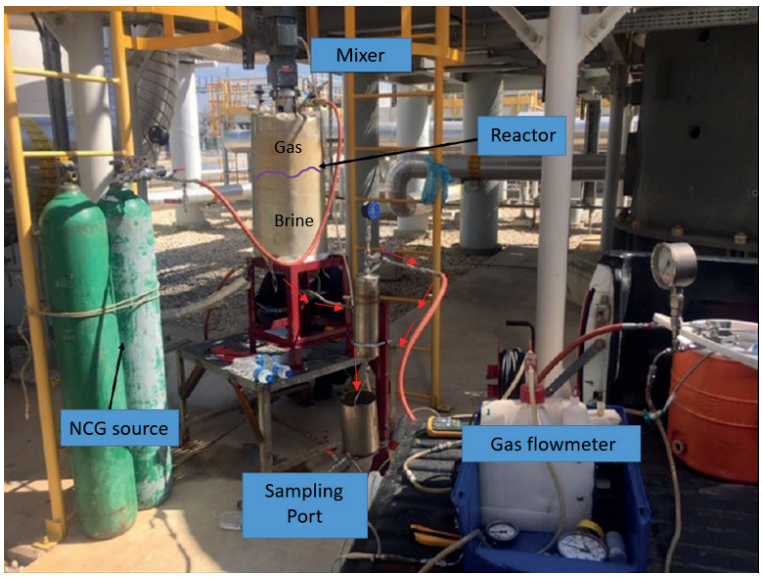

Figure 8. A view of the experimental setup in the field.
Şekil 8. Sahada kurulan deney sisteminin görünümü.

Table 3. Gas content of NCG.
Çizelge 3.Yoğuşmayan gazların (YMG) bileşimi.

Gas Composition	Volume % in dry gas
Carbon Dioxide (CO_2)	99.38
Nitrogen (N_2)	0.36
Methane (CH_4)	0.21
Hydrogen Sulfide (H_2S)	0.0036
Argon (Ar)	0.003
Hydrogen (H_2)	0.01
Helium (He)	0.00005

Table 4. Concentration of elements in geothermal brine.
Çizelge 4. Jeotermal akışkandaki element konsantrasyonları.

Element	Concentration (ppm)	Element	Concentration (ppm)
F^-	10.3	Na^+	606.6
Cl^-	306	NH_4^+	6.3
Al^{3+}	0.43	K^+	47.7
Br^-	1.35	Mg^{+2}	0.52
NO_3^-	1.06	Ca^{+2}	21
SO_4^{-2}	19.8	CO_3^{-2}	320
PO_4^{-3}	1.4	HCO_3^-	160
Li^+	4.0	Si^{+4}	120
TDS	1627		

Modeling of Batch Experiments using PHREEQC

PHREEQC version 3 (PH Redox Equilibrium), which has the capability to perform saturation index calculations and speciation, was used for aqueous geochemical calculations (Parkhurst and Appelo, 2013). PHREEQC may also be used to study mineral and gas equilibria, solution mixing, advective transport calculations, inverse modeling, surface complexation reactions, and ion exchange reactions (Parkhurst, 2005). PHREEQC can utilize different

thermodynamic databases, such as the default database LLNL (Parkhurst and Appelo, 2013) or Thermoddem developed by Blanc et al. (2012). Due to the degree of crystallinity and/or the compositions of the examined mineral phases, the choice of thermodynamic dataset utilized in the calculations is a case-by-case procedure, and the various thermodynamic datasets can result in different outcomes. Akin and Kargı (2019) simulated the geochemical evolution of fluids in geothermal wells in the west of Türkiye using PHREEQC code. They used databases such as PHREEQC.dat and LLNL.dat when matching actual field measurements. The use of LLNL.dat provided a better match with the field's geochemical data. Since similar compositions of geothermal fluid have been used in this study, LLNL.dat was utilized as the reference database for the simulation of CO_2 dissolution. A code written in the PHREEQC Notepad was used for CO_2 dissolution in geothermal water and water-rock interaction. CO_2 solubility in water was solved using the Peng-Robinson equation of state (Peng & Robinson, 1976). Governing equations for water-rock interactions are presented in Equations 1 to 4. In these equations, activation energy (E) is the minimum amount of energy required for a chemical reaction to occur. Activation energy determines the rate at which mineral reactions, such as dissolution or precipitation, occur. The higher the energy activation, the slower the reaction rate at a given temperature. Kinetic reaction rates ($k_{1,2}$) describe how quickly a chemical reaction proceeds over time. For minerals, this refers to the rates at which they dissolve in a solvent or precipitate from a solution. The rate of these reactions depends on several factors, including temperature, energy activation, mineral surface area, and ionic strength.

$$k_2 = k_1 * \exp\left(\frac{E}{R} * \left(\frac{1}{T_K} - \frac{1}{298.15}\right)\right) \quad (1)$$

$$\left(\frac{A_0}{V}\right) * \left(\frac{m}{m_0}\right)^{0.67} * k_2 * (1 - SR(\text{Mineral})) \quad (2)$$

$$Moles = rate * time \quad (3)$$

$$Concentration = moles * MW * 1000 \quad (4)$$

RESULTS AND DISCUSSION

The mineral surface area A_0 was determined through image processing with ImageJ, supplemented by SEM-EDX and XRD results. XRD analyses of core samples were conducted using a GNR APD 2000PRO brand X-ray diffractometer. Core samples from depths of 1900 m and 3000 m were crushed and sorted using screeners (Figure 9).

The image processing of rock powders was conducted using ImageJ. An image of randomly mixed mineral particles was captured and introduced to ImageJ (Figure 10). By coloring the mineral particles, image processing provides volume and surface area of minerals by utilizing the roundness and size of the particles (Figure 11). The average particle area was measured as 0.398 mm² with a standard deviation of 0.167 mm². To determine the mineral surface area of each mineral type, it is necessary to obtain measurements using a polarized light microscope. (Figures 12 and 13), EDX SEM (Figures 16 and 17, Tables 5 and 6), and XRD analyses (Figures 16 and 17). The major minerals identified with EDX SEM included quartz, albite, magnesite, siderite, kaolinite, calcite, and muscovite.

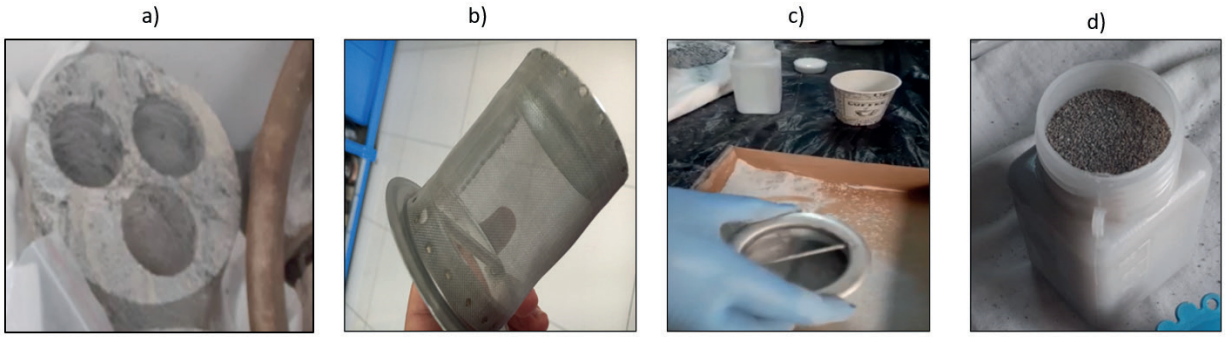

Figure 9. Crushing core samples into small particles (core sample (a) Screener (b), shaking screeners (c), separated particles (d)).

Şekil 9. Karot örneklerinin küçük partiküllere kırılması (a) karot örneği, (b) elek, (c) titreşimli elekler, (d) seçilen partiküller.

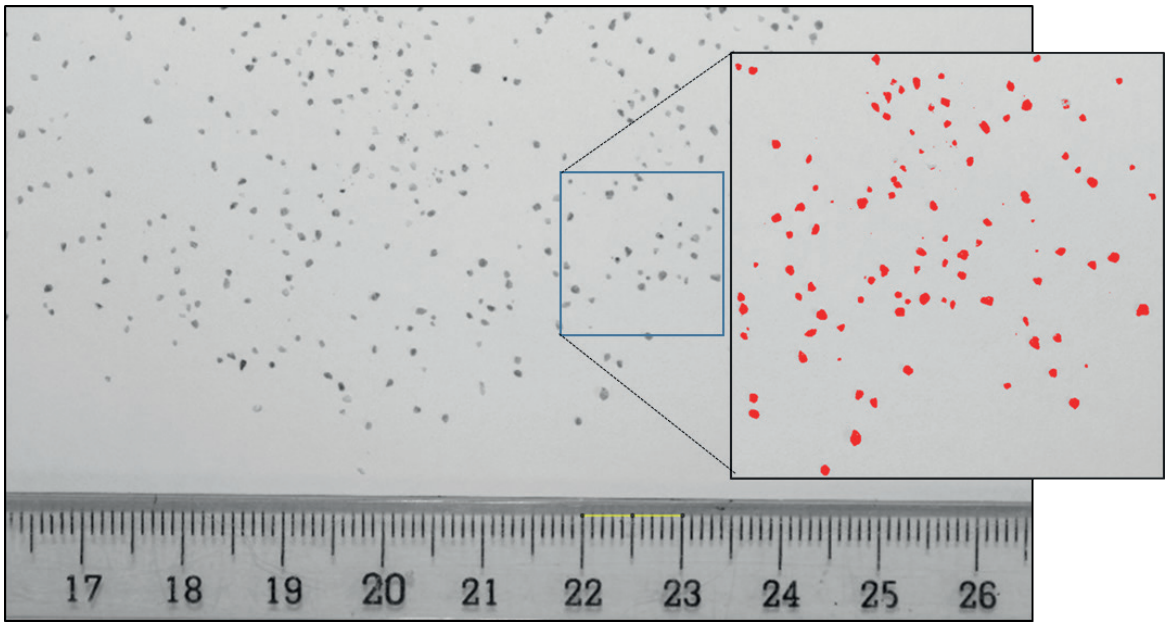

Figure 10. Image processing of rock powder using ImageJ.

Şekil 10. ImageJ ile kaya tozu partiküllerinin görüntü analizleri.

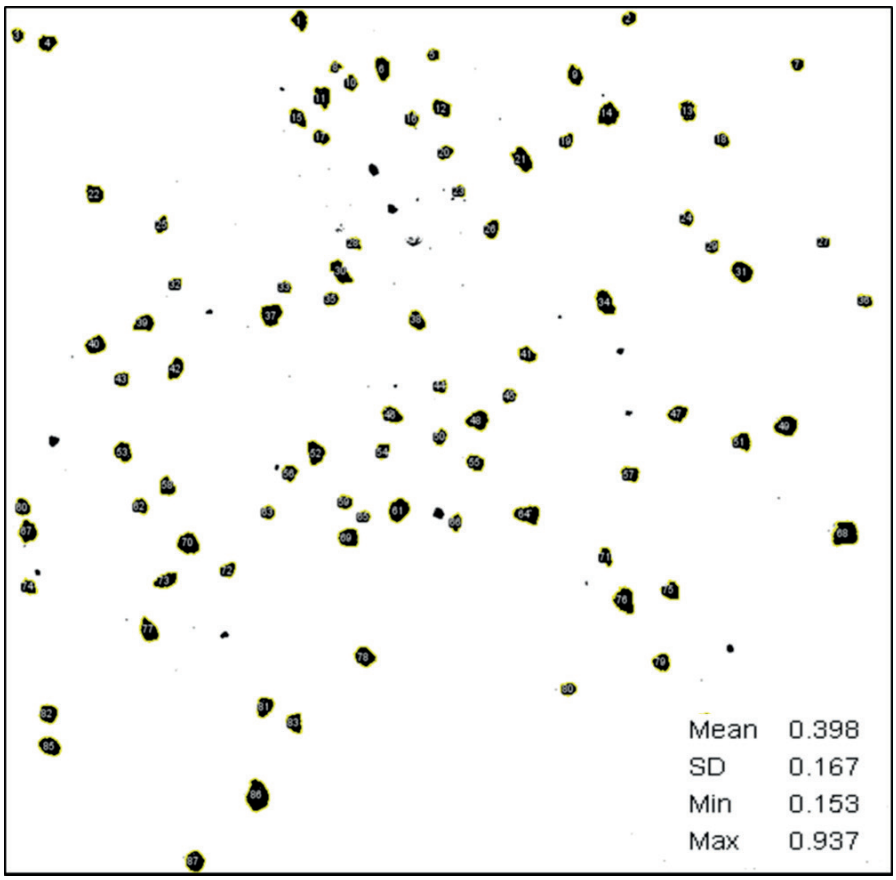

Figure 11. Mineral surface area (in mm^2) calculation using ImageJ.
Şekil 11. ImageJ tabanlı mineral yüzey alanı (mm^2) hesaplaması.

The samples were crushed into powder and placed on the plaques. XRD patterns were then obtained and interpreted to identify mineral content. The mineral contents of the powder were calculated by matching peak measurements with the Inorganic Crystal Structure Database (ICSD) 12++ dataset. The XRD results for two sets of mineral assemblages before and after the batch experiments are shown in Figures 16 and 17. PHREEQC software was used to simulate water-rock interaction in the batch experiments. The average mineral surface area, calculated with the ImageJ program, was then multiplied by the mineral content of each mineral to obtain their corresponding surface areas separately.

Equations (5) to (13) provide standard stoichiometric reactions. The CO_2-charged geothermal water reacts with rock minerals in two ways. First, it consumes hydrogen ions that neutralize the acidic gas-charged water, thereby increasing the likelihood of carbonate mineral precipitation as the pH rises. Second, the cations react with dissolved CO_2 to form stable carbonate minerals.

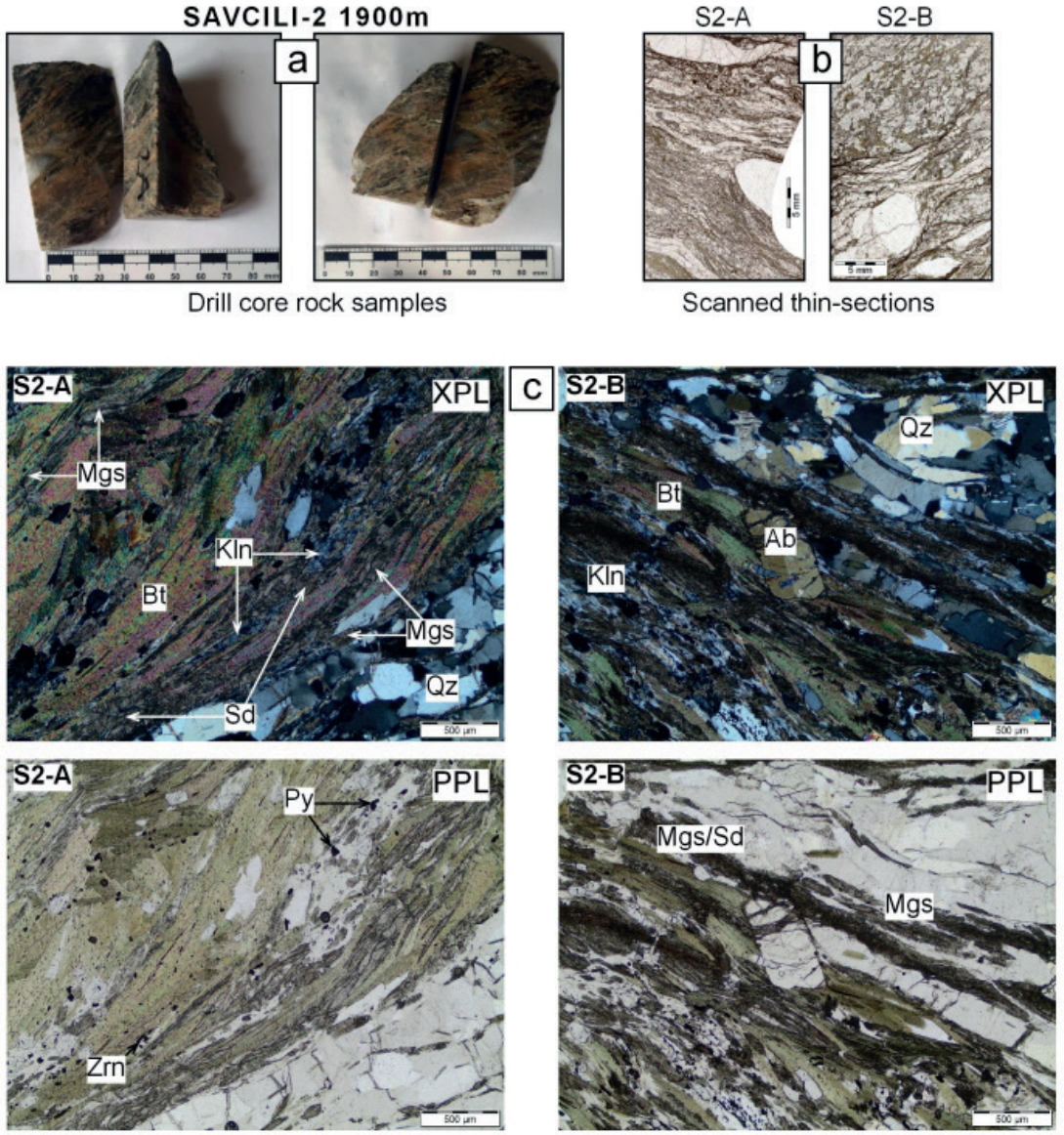

Figure 12**.** a) Macroscopic view of the core sample taken from 1900 m depth, b) polarized light microscope measurements identified quartz-filled lenses and bands, c) lepidoblastic biotite and granoblastic quartz and albite minerals, and alteration products magnesite (Mgs), siderite (Sd) and kaolinite (Kln) developed between biotite plates. XPL: Double Nicol, PPL: Single Nicol, Mgs: Magnesite, Sd: Siderite, Qz: Quartz, Bt: Biotite, Ab: Albite, Zrn: Zircon Py: Pyrite.

Şekil 12. a) 1900 m derinlikten alınan karot örneğinin makroskobik görünümü b) Polarizan ışık mikroskobu ölçümlerinde kuvars dolgulu lens ve bantlar tanımlanmıştır c) Lepidoblastik biyotit ile granoblastik kuvars ve albit mineralleri, ayrıca alterasyon ürünleri olan manyezit (Mgs), siderit (Sd) ve biyotit lamelleri arasında gelişmiş kaolinit (Kln) mineralleri gözlenmiştir.XPL: Çift nikol, PPL: Tek nikol, Mgs: Manyezit, Sd: Siderit, Qz: Kuvars, Bt: Biyotit, Ab: Albit, Zrn: Zirkon, Py: Pirit.

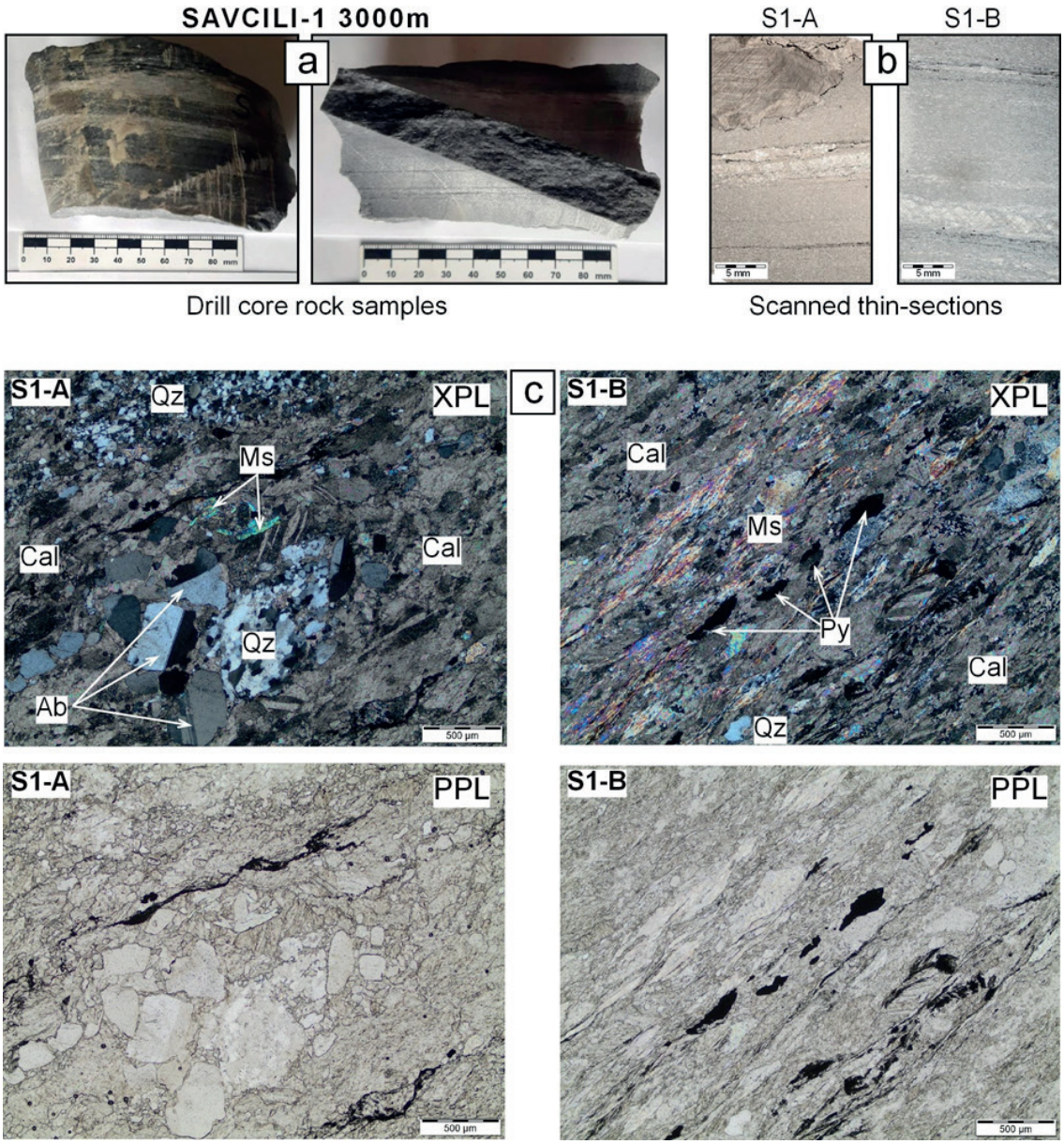

Figure 13. a) Macroscopic view of the core sample taken from 3000 m depth, (b) calcite-filled lens and quartz-filled bands in polarized light microscope measurements, (c) optical microscope views of levels containing granoblastic textured calcites and quartz, albite, muscovite and opaque mineral (pyrite). XPL: Double Nicol, PPL: Single Nicol, Cal: Calcite, Qz: Quartz, Ms: Muscovite, Ab: Albite, Py: Pyrite.

Şekil 13. a) 3000 m derinlikten alınan karot örneğinin makroskobik görünümü b) Polarizan ışık mikroskobu (PLM) incelemelerinde kalsit dolgulu lens ve kuvars dolgulu bantlar gözlenmiştir c) Granoblastik dokulu kalsitlerin yanı sıra kuvars, albit, muskovit ve opak mineral (pirit) içeren seviyelerin optik mikroskop görüntüleri. XPL: Çift nikol, PPL: Teknikol, Cal: Kalsit, Qz: Kuvars, Ms: Muskovit, Ab: Albit, Py: Pirit.

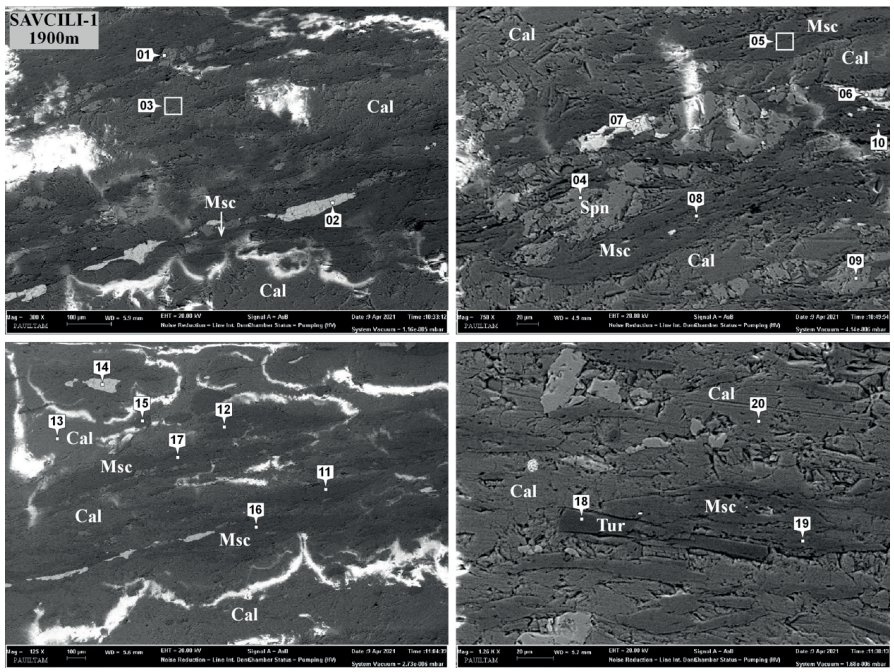

Figure 14. EDX SEM images of rock samples from 1900 m depth.

Şekil 14. 1900 m derinliğindeki kaya örneklerinin EDX-SEM görüntüleri.

Table 5. Chemical formulas of minerals at 1900 m.

Çizelge 5. 1900 m derinliğinde tanımlanan minerallerin kimyasal bileşimleri.

1	Sphene (Titanite)	$CaTiSiO_5$
2	Chloritized biotite	$K_{0.6}(Si_{3.5}Al_{0.5})\ (AI_{2.5}Mg_{2.2}Fe_{0.1})\ O_{10}(OH)_8$
3	Calcite	$CaCO_3$
4	Sphene (Titanite)	$CaTiSiO_5$
5	Phengitic muscovite	$(K_{0.6}Na_{0.2}Ca_{0.1})\ (Si_{3.1}AI_{0.9})\ (AI_{1.5}Mg_{0.8})\ O_{10}(OH)_2$
6	Apatite	$Ca_{5.0}(PO_4)_3(OH)_{0.3}F_{0.3}CI_{0.3}$
7	Pyrite	FeS_2
8	Phengitic muscovite	$(K_{0.6}Na_{0.2}Ca_{0.1})\ (Si_{3.1}AI_{0.9})\ (AI_{1.5}Mg_{0.8})\ O_{10}(OH)_2$
9	Sphene (Titanite)	$CaTiSiO_5$
10	Phengitic muscovite	$(K_{0.6}Na_{0.2})\ (Si_{3.1}AI_{1.0})\ (AI_{1.5}Mg_{0.8})\ O_{10}(OH)_2$
11	Phengitic muscovite	$(K_{0.6}Na_{0.1})\ (Si_{3.1}AI_{0.9})\ (AI_{1.5}Mg_{0.8})O_{10}(OH)_2$
12	Phengitic muscovite	$(K_{0.7})\ (Si_{3.0}AI_{1.0})\ (AI_{1.3}Mg_{1.3}Fe_{0.1})\ O_{10}(OH)_2$
13	Calcite	$CaCO_3$
14	Pyrite	FeS_2
15	Quartz	SiO_2
16	Phlogopite	$(K_{0.7})\ (Si_{3.0}AI_{1.0})\ (AI_{1.0}Mg_{1.7}Fe_{0.1})\ O_{10}\ (OH)_2$
17	Phlogopite	$(K_{0.6}Na_{0.2})\ (Si_{3.0}AI_{1.0})\ (AI_{1.1}\ Mg_{1.4}Fe_{0.1})\ O_{10}(OH)_2$
18	Tourmaline	$NaMg_{3.0}AI_{6.0}(BO_3)_3Si_6O_{18}(OH)_4$
19	Phengitic muscovite	$(K_{0.7})\ (Si_{3.1}AI_{0.9})\ (AI_{1.6}Mg_{0.7}Fe_{0.1})\ O_{10}\ (OH)_2$
20	Calcite	$CaCO_3$

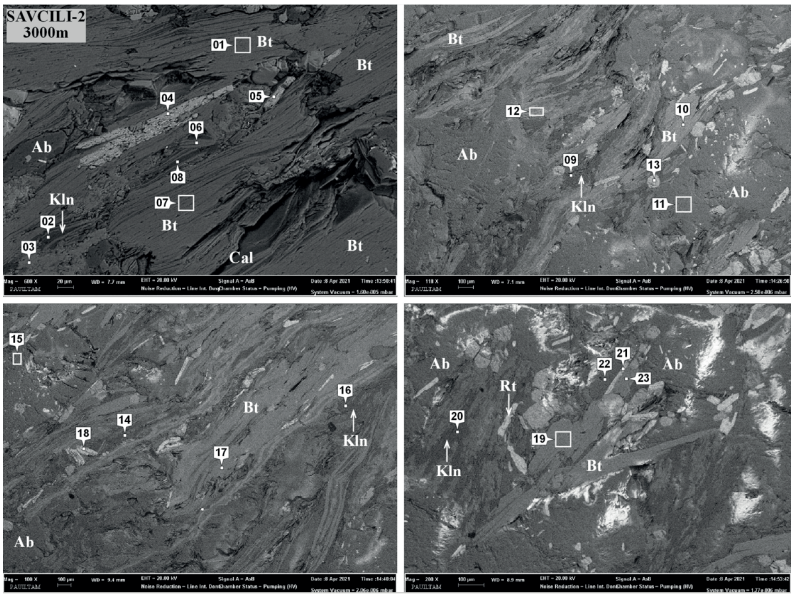

Figure 15. EDX SEM images of rock samples from 3000 m depth.

Şekil 15. 3000 m kaya örneklerinin EDX-SEM görüntüleri.

Table 6. Chemical formulas of minerals at 3000 m.

Çizelge 6.3000 m derinliğinde tanımlanan minerallerin kimyasal bileşimleri.

1	Biotite	$(K_{0.9})\ (Si_{3.0}AI_{1.0})\ (Mg_{2.1}Fe_{0.8}AI_{0.2})\ O_{10}\ (OH)_2$
2	Kaolinite	$Si_2AI_2O_5\ (OH)_4$
3	Ferroan Magnesite	$((Mg, Fe)_2CO_3)$
4	Ilmenite	$(Fe^{2+}TiO_3)$
5	Ilmenite	$(Fe^{2+}TiO_3)$
6	Biotite	$(K_{0.7}\ Na_{0.1})\ (Si_{3.0}AI_{1.0})\ (Mg_{2.0}Fe_{0.6}AI_{0.3})\ O_{10}\ (OH)_2$
7	Biotite	$(K_{0.8})\ (Si_{3.0}AI_{1.0})\ (Mg_{2.1}Fe_{0.6}AI_{0.4})\ O_{10}\ (OH)_2$
8	Kaolinite	$Si_2AI_2O_5\ (OH)_4$
9	Kaolinite	$Si_2AI_2O_5\ (OH)_4$
10	Biotite	$(K_{0.7})\ (Si_{3.0}AI_{1.0})\ (Mg_{2.2}Fe_{0.3}AI_{0.5})\ O_{10}\ (OH)_2$
11	Feldspar	$Na_{1.0}AI_{1.0}Si_{3.0}O_8$
12	Calcian magnesian siderite	$(Ca,Mg,Fe)_2CO_3$
13	Apatite	$Ca_{5.0}(PO_4)_3(OH)_{0.3}F_{0.3}CI_{0.3}$
14	Kaolinite	$Si_2AI_2O_5(OH)_4$
15	Feldspar	$Na_{0.9}Ca_{1.0}\ AI_{1.1}Si_{2.9}O_8$
16	Kaolinite	$Si_2AI_2O_5(OH)_4$
17	Biotite	$(K_{0.9})\ (Si_{3.0}AI_{1.0})\ (Mg_{2.1}Fe_{0.8}AI_{0.2})\ O_{10}\ (OH)_2$
18	Rutile	TiO_2
19	Biotite	$(K_{0.7})\ (Si_{3.0}AI_{1.0})\ (Mg_{2.3}Fe_{0.2}AI_{0.5})\ O_{10}\ (OH)_2$
20	Kaolinite	$Si_2AI_2O_5(OH)_4$
21	Ilmenite	$Fe^{2+}TiO_3$
22	Feldspar	$Na_{1.0}AI_{1.0}Si_{3.0}O_8$
23	Biotite	$(K_{0.6}\ Na_{0.2})\ (Si_{3.0}AI_{1.0})\ (Mg_{2.2}Fe_{0.6}AI_{0.3})\ O_{10}\ (OH)_2$

The representative reaction for this process is depicted in Equation (5) (Delerce et al., 2023). These cations facilitate the mineralization of CO_2 (g) into biotite, calcite, and kaolinite. In the first mineral assemblage at a depth of 1900 m, the quartz mineral content decreased from 19.4% to 15.3%; magnesite mineral content remained unchanged; kaolinite mineral content increased from 13.2% to 15.7%; and biotite content rose from 3.6% to 4.3%. Dolomite mineral content decreased by half of its initial value, and siderite content fell from 1.5% to 0.4% (Figure 16). In the second mineral assemblage at 3000 m depth, the calcite content increased from 66.6% to 79.1%; the quartz content decreased from 20.3% to 13%; and the muscovite mineral content decreased from 13.1% to 7.9% (Figure 17). Alteration involves the decomposition of primary metamorphic rock and the precipitation of secondary minerals. In the batch experiments, the mineral assemblage remained constant while the abundance of the minerals changed. Equations (6) and (7) represent the carbonation of siderite (Mendoza et al., 2019), while equation (8) describes the reaction of pyrite with water and oxygen to form sulfuric acid. Magnesite carbonation is expressed in equations (9) and (10). Metal cations in the minerals are exchanged for H^+, resulting in the release of metal cations (K^+, Ca^{2+}, Na^+, etc.), and the content of smectite and kaolinite may increase from the retained ions (AI^{3+}, O^{2-}, Si^{4+}) (Mendoza et al., 2019). The hydrolysis of calcium plagioclase feldspar and potassium feldspar is illustrated in equations (11) and (12), and equation (13) depicts the alteration of albite into muscovite. During sampling and handling, CO_2 may degas even with minimal exposure, leading to localized increase in pH within specific microenvironments. This change could temporarily raise the calcite saturation index, promoting its precipitation. Certain mineral phases, especially secondary kaolinite, may have formed during cooling or after the experiment in the drying phase. These are limitations of the experiments.

$$2H^+ + H_2O + (Ca, Mg, Fe, Al)SiO_3 \rightarrow Ca^{2+}, Mg^{2+}, Fe^{2+}, Al^{3+} + H_4SiO_4 \quad (5)$$

$$Fe_3O_4(s) + Fe(s) + 4CO_2(g) \rightarrow 4FeCO_3\,(s) \quad (6)$$

$$Fe_2O_3(s) + Fe(s) + 3CO_2(g) \rightarrow 3FeCO_3\,(s) \quad (7)$$

$$2FeS_2(s) + 7O_2 + 2H_2O \rightarrow 2Fe^{2+} + H_2SO_4 + 2H^+ \quad (8)$$

$$Mg^{2+}(aq) + 2HCO_3^-(aq) \rightarrow MgCO_3\,(s) + CO_2\,(g) + H_2O \quad (9)$$

$$Mg(OH)_2 + 2CO_2 \rightarrow Mg(HCO_3)_2 \quad (10)$$

$$KAlSi_3O_8 + H^+ + 4.5H_2O \rightarrow 0.5\,Al_2Si_2O_5(OH)_4 + K^+ + 2H_4SiO_4(aq) \quad (11)$$

$$CaAl_2Si_2O_8 + H_2CO_3 + 0.5O_2 \rightarrow Al_2Si_2O_5(OH)_4 + Ca^{2+} + CO_3^{2-} \quad (12)$$

$$3NaAlSi_3O_8 + K^+ + 2H^+ \rightarrow KAl_3Si_3O_{10}(OH)_2 + 3Na^+ + 6SiO_2 \quad (13)$$

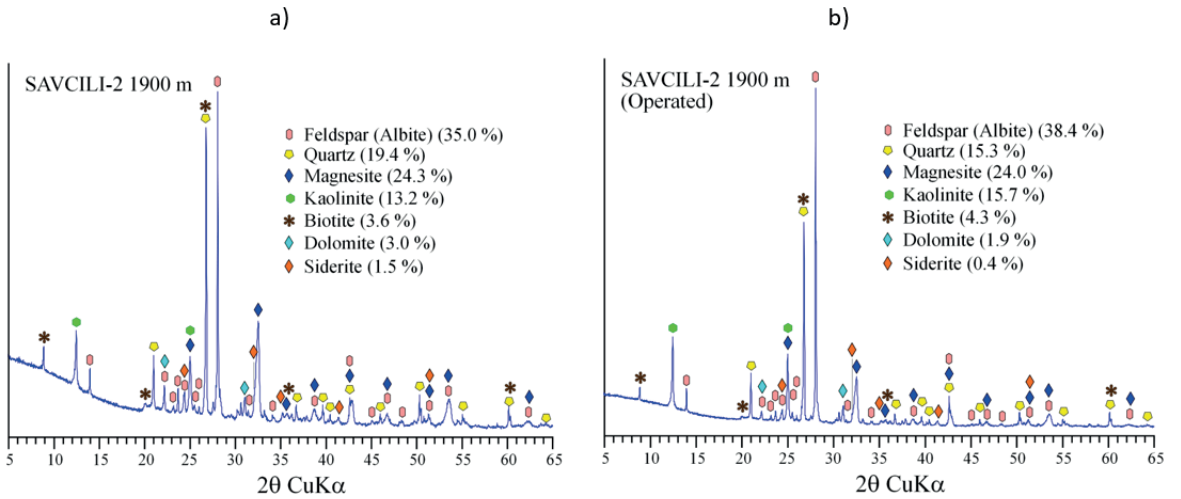

Figure 16. XRD measurements of the core sample taken from 1900 m depth before (a) and after (b) batch experiments.
Şekil 16. 1900 m derinlikten alınan karot örneğinin kesikli deneyleri öncesi (a) ve sonrası (b) XRD ölçümleri.

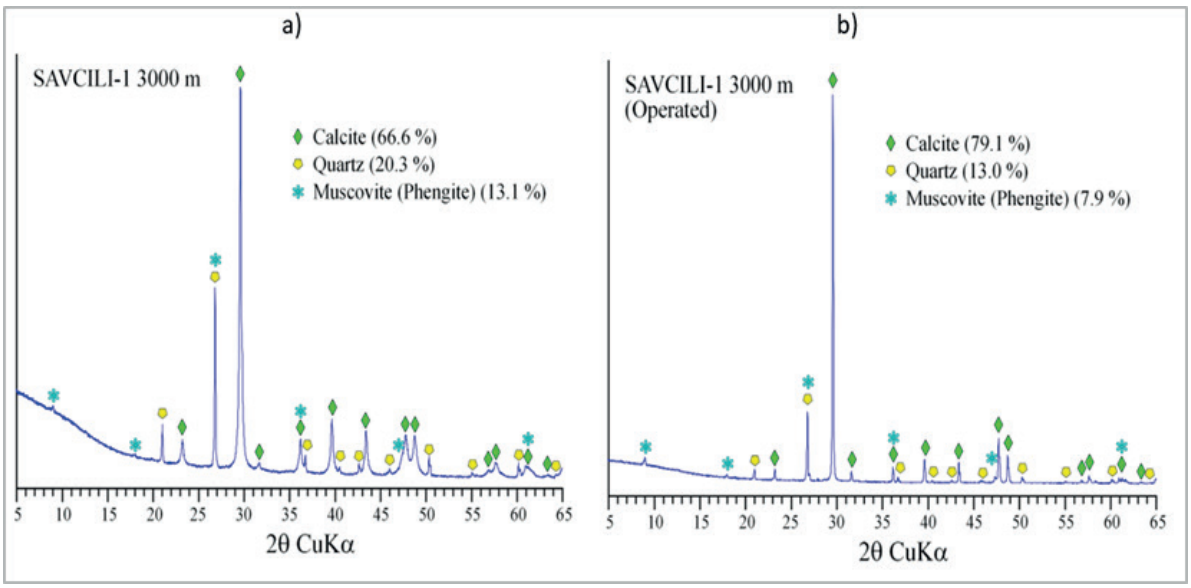

Figure 17. XRD measurements of the core sample taken from 3000 m depth before (a) and after (b) batch experiments.
Şekil 17. 3000 m derinlikten alınan karot örneğinin kesikli deneyleri öncesi (a) ve sonrası (b) XRD ölçümleri.

A PHREEQC code was used to simulate the batch experiment, considering rock surface area, initial moles of minerals, kinetic reaction rates, and activation energy of the minerals. The number of moles and rock surface area for each mineral were calculated using the image processing method and XRD results (Tables 7 and 8). By tuning the kinetic rates and activation energy of the minerals, ion concentrations (SiO_2, Ca^{2+}, Al^{3+}, Cl^-, and Fe^{2+}) were adjusted to match experimental results (Table 7). Concentrations of major elements were aligned with those obtained from experimental results (Figures 18-21). The parameters were consistent with USGS data (Table 9).

It is recognized that calibrating both kinetic rates and activation energy parameters adds flexibility, which, if not carefully constrained, could weaken the model's predictive accuracy. To mitigate this risk, our calibration strategy was informed by literature values, particularly those reported by Palandri and Kharaka (2004), which served as limits for both kinetic rates and activation energies. The tuning process was conducted within these published ranges, prioritizing adjustments to only one parameter (usually the kinetic rate) unless a good match could not be achieved. In such cases, minimal adjustments to the activation energy were made to better align with experimental data while maintaining physical plausibility.

Additionally, the calibration was validated by reproducing multiple elemental concentration trends (e.g., SiO_2, Ca^{2+}, Fe^{2+}), not just a single target variable, which helps reduce the risk of parameter compensation and overfitting.

Table 7. Surface area and mole number of mineral assemblages for the rock sample taken from a depth of 1900 m.

Çizelge 7. 1900 m derinliğindeki kaya örneğinde belirlenen mineral topluluklarının yüzey alanı ve mol miktarları.

Minerals	Mole number	Mineral surface area (cm^2)
Feldspar	0.226	1451.9
Quartz	0.581	804.8
Magnesite	0.518	1008.0
Kaolinite	0.092	547.6
Biotite	0.0149	149.3
Dolomite	0.029	124.5
Siderite	0.023	62.2

Table 8. Surface area and mole number of mineral assemblages for rock sample taken from 3000 m depth.

Çizelge 8. 3000 m derinlikten alınan kaya örneğine ait mineral topluluklarının yüzey alanı ve mol sayısı.

Minerals	Mole number	Mineral surface area (cm^2)
Calcite	1.118	2578.5
Quartz	0.570	786.0
Muscovite	0.068	507.2

In the first batch experiment, a mineral assemblage comprising rock powder obtained from a core sample taken at a depth of 1900 m was exposed to CO_2-saturated brine for 3 weeks at 95 °C and 10 bar. Due to the constraints associated with sealing the experimental batch tank, the pressure in the experiments was limited to 10 bar. To accurately simulate reservoir conditions, we utilized PHREEQC software. The concentration of major elements was matched with simulations by tuning the activation energy and kinetic reaction rate of minerals.

Table 9. Activation energy and kinetic rate constant to match PHREEQC model with experimental results and USGS values.

Çizelge 9. PHREEQC modelinin deney sonuçları ve USGS değerleriyle uyumlandırılması için kullanılan aktivasyon enerjisi ve kinetik hız sabiti.

	Activation Energy (kJ mol^{-1})		**Kinetic Rate constants (mol m^{-2} s^{-1})**	
	PHREEQC Model	USGS (Palandri & Kharaka, 2004)	PHREEQC Model	USGS (Palandri & Kharaka, 2004)
Quartz	77	87.7	9×10^{-14}	1.023×10^{-14}
Muscovite	22	22	1.404×10^{-13}	2.81×10^{-14}
Pyrite	57	56	8.81×10^{-6}	2.8×10^{-5}
Albite	69	69	2.75×10^{-10}	2.754×10^{-13}
Kaolinite	22	38	6×10^{-11}	1.1×10^{-14}
Dolomite	36	52	6.45×10^{-9}	2.95×10^{-8}
Magnesite	20	23.5	4×10^{-10}	4.5×10^{-10}
Siderite	65	62.7	9×10^{-8}	1.26×10^{-9}
Calcite	20	23.5	9×10^{-9}	1.55×10^{-9}

As seen in Figure 15a, antimony concentration increased from 0.3 ppm to 1.1 ppm. Antimony, a constituent of hydrothermally-formed mineral pangenesis, is often found in the trivalent state as stibnite (Sb_2S_3) (Krupp, 1988). Stibnite is the most abundant mineral for antimony and serves as the primary control over the concentration of antimony in hydrothermal fluid (Olsen et al., 2012). Antimony's sulfur solubility is very sensitive to temperature and pH changes (Erten et al., 2021). In general, stibnite is more soluble in acidic solutions than in basic solutions. This is because the sulfide ion (S^{2-}) is more stable in acidic solutions. In basic solutions, the sulfide ion can react with hydroxide ions (OH) to form insoluble hydroxides. The following reaction shows the oxidation of stibnite in an acidic solution:

$$Sb_2S_3 + 3H_2O + 3O_2 \rightarrow 2Sb(OH)_3 + 3H_2S \quad (14)$$

CO_2 dissolution in the geofluid decreases the pH from 9.5 to 7.2. Thus, the reaction in Eq. (14) shifted to the right and increased the antimony concentration.

Al^{3+} decreased from 0.43 ppm to 0.15 ppm (Figure 18b). The source of Al^{3+} was the kaolinite mineral in the rock sample. The precipitation of kaolinite (increasing the mineral content from 13.1% to 15.7%) resulted in a decline in Al^{3+} (Figure 16). Kaolinite is a clay mineral that is relatively insoluble in water. However, its solubility increases as pH decreases. This occurs because the negative charges on the surface of the kaolinite particles are more easily balanced by hydrogen ions (H^+) in acidic solutions (Rao et al., 2011). Kaolinite is also more reactive to acid at lower pH values because acid can break the bonds between the silicon and oxygen atoms in the kaolinite structure. In the experiment, the pH value falls within the alkaline range, which is unfavorable for alkaline solubility.

Table 10. Solubility of kaolinite with respect to pH (Derived from Rao et al., 2011).

Çizelge 10. Kaolinit çözünürlüğünün pH ile ilişkisi (Rao vd., 2011'den türetilmiştir).

pH	Solubility	Reactivity	Stability
Acidic (<4)	High	High	Low
Neutral (4-7)	Low	Low	High
Alkaline (>7)	Very low	Very low	High

Fe^{2+} levels dropped from 0.1 ppm to stabilize at 0.02 ppm (Figure 18c). The Fe^{2+} source in this experiment is attributed to the presence of siderite and biotite minerals. XRD analysis indicated that siderite was dissolving, while biotite precipitated (Figure 16). The solubility of siderite ($FeCO_3$) in water diminishes as pH increases, as siderite is a slightly acidic compound whose solubility is enhanced under acidic conditions (Silva et al. 2002). Equation (15) illustrates the dissolution of siderite in water:

$$FeCO_3\,(s) + H_2O\,(l) + CO_2\,(g) \Leftrightarrow Fe^{2+}\,(aq) + HCO_3^-\,(aq) \quad (15)$$

The solubility of siderite is also affected by the temperature and ionic strength of the solution (Bénézeth et al., 2009). The solubility of siderite decreases with rising temperature and ionic strength.

Table 11. Solubility of siderite with respect to pH (Silve et al., 2002).

Çizelge 11. Siderit çözünürlüğünün pH ile ilişkisi (Silve vd., 2002).

pH	Temperature (ºC)	Solubility (mg L^{-1})
5	25	100
6	25	50
7	25	10
8	25	0.1

Biotite is a mica mineral commonly found in igneous, metamorphic, and sedimentary rocks. It is a sheet silicate mineral, meaning its structure consists of layers of silicon dioxide (SiO_2) sandwiched between layers of aluminum, iron, magnesium, and potassium (Samadi et al., 2021). Generally, biotite dissolves more rapidly in acidic solutions than in basic ones. This is because acidic solutions can more easily break the bonds that hold the minerals together (Bray et al., 2015). The solubility of biotite in water decreases with increasing temperature, as higher temperatures provide more energy for water molecules to break the bonds holding the biotite mineral together (Malmström and Banwart, 1997). In the experiment, the initial temperature was 25 °C, which increased to 95 °C and stabilized throughout the experiment. Thus, biotite exhibited precipitation behavior, resulting in a decrease in Fe^{2+}.

The concentration of Ca^{2+} showed a declining trend during the experiment (Figure 18d). $CaCO_3$ is more soluble in water at lower pH levels, indicating that it dissolves more readily in acidic environments (Hart et al., 2013). This occurs because the carbonate ion (CO_3^{2-}) is more stable in acidic conditions. Additionally, the solubility of Ca^{2+} in water decreases as the temperature rises (Straub, 1932), meaning that less Ca will dissolve in warm water compared to cold. In this experiment, dolomite served as the source of Ca^{2+}. As illustrated in Figure 16, the dolomite concentration dropped from 3.0% to 1.9%. Several factors influence the solubility of dolomite, including temperature, pH, and the presence of other ions, with temperature being the most impactful. Dolomite's solubility in water is influenced by pH; it increases with rising pH levels, suggesting that more dolomite will dissolve in basic solutions due to the carbonate ion (CO_3^{2-}), the primary element in dissolved

dolomite, being more stable in such conditions. However, increased temperature results in a decrease in dolomite solubility, as the amount that dissolves in hot water is less than in cold water. The pH in the experiment fell from 9.5 to 7.2 (Figure 19d), which would typically suggest an increase in Ca^{2+} solubility. Nonetheless, the system's temperature elevated from 25 °C to 95 °C, leading to a reduction in Ca^{2+} solubility.

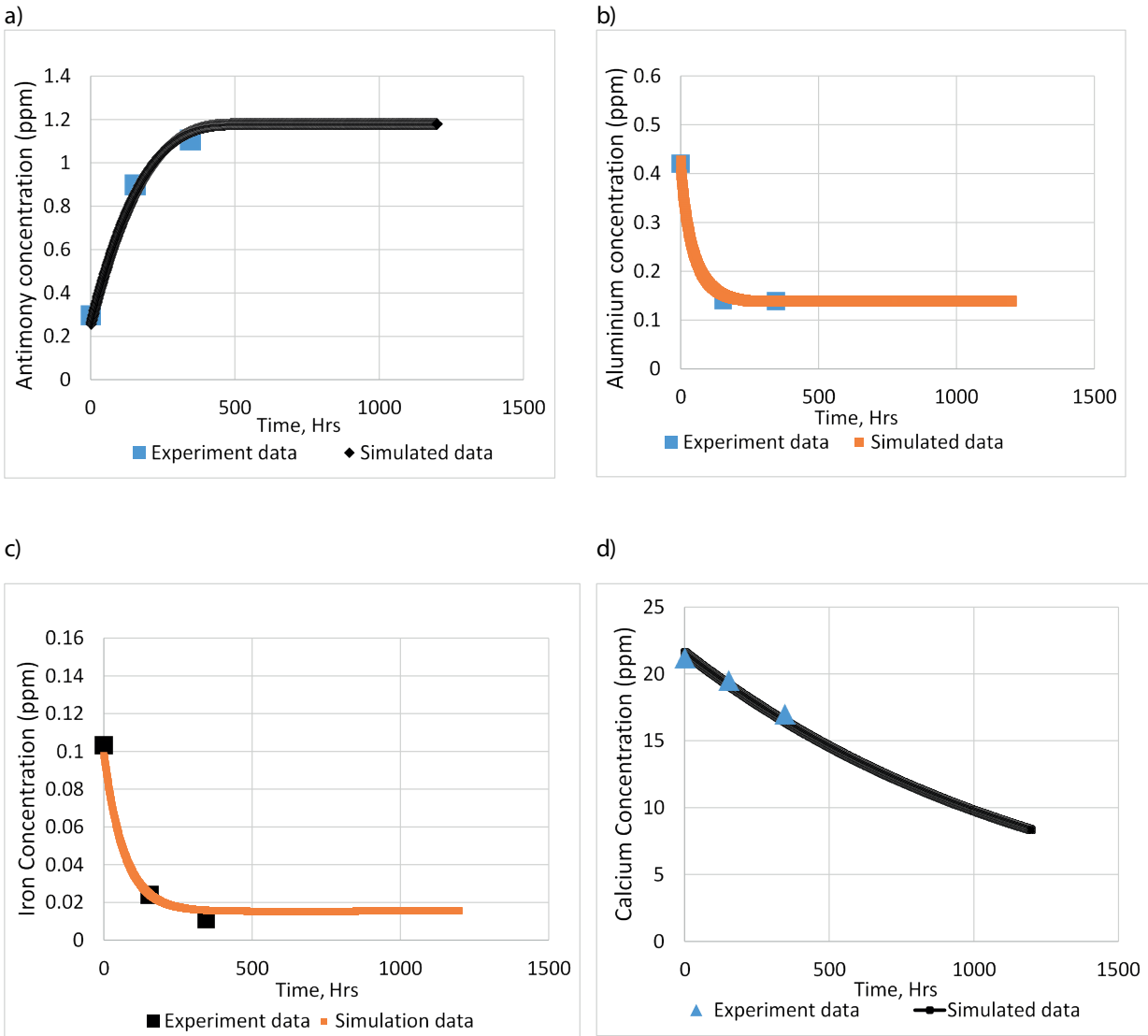

Figure 18. Experimental and simulation results for rock samples taken from 1900 m, a) antimony, b) aluminum, c) Fe^{2+}, d) Ca^{2+}

Şekil 18. 1900 m derinlikten alınan kaya örneklerine ait deney ve simülasyon sonuçları: a) antimon b) alüminyum c) Fe^{2+} d) Ca^{2+}

Silica concentration decreased from 120 ppm to 85 ppm (Figure 19a). The solubility of silica in water is little affected by pH values between 1 and 9, but rises rapidly at pH levels above 9 (Krauskopf, 1956). Consequently, it is not influenced by the pH of the water. The solubility of silica is also impacted by temperature; it increases with rising temperature (Krauskopf, 1956). This is because water molecules can more easily break apart silica molecules at higher temperatures. Additionally, the solubility of SiO_2 is influenced by the presence of other ions in water. For example, the presence of Ca^{2+} can reduce the solubility of SiO_2. This occurs because Ca^{2+} can form complexes with silica molecules, making them less soluble in water (Szymanek et al., 2021).

Mg^{2+} concentration increased from 0.8 to 5 ppm (Figure 19b). The source of magnesium was magnesite and dolomite minerals in the experiment. The presence of magnesite at 1900 m depth was confirmed by consistent XRD peaks and further validated through SEM-EDS spot analyses. The core sample from this depth was classified as a biotite-quartz-albite schist, a typical lithology of the Menderes metamorphic complex. Therefore, the magnesite detected does not have primary igneous origin but is interpreted as a post-metamorphic alteration product formed during low-temperature (<200 °C) hydrothermal processes related to geothermal fluid circulation. This interpretation aligns with previous studies of metamorphic rocks in the region, where magnesite and siderite often occur as pore-filling carbonates or thin alteration bands (Haklıdır et al., 2021; Karamanderesi & Helvaci, 2003; Bozkaya et al., 2024). Magnesite content decreased from 24.3% to 24% and dolomite mineral content decreased from 3.0% to 1.9% (Figure 16).

The Cl concentration remained constant, stabilizing around 145 ppm (Figure 19c). The solubility of chloride ions in water is unaffected by pH. Cl ions are negatively charged, while pH measures the concentration of H^+ in a solution. Solubility of Cl is influenced by temperature, but not by pH (Musa & Hamoshi, 2012).

In the second batch experiment, a mineral assemblage comprising rock powder obtained from a core sample taken from a depth of 3000 m was exposed to CO_2-saturated brine for 3 weeks at 95 °C and 10 bar. The mineral content of the rock sample is shown in Figure 17.

Mg^{2+} concentration showed an increasing trend (Figure 20a). The solubility of Mg^{2+} increases with rising pH, indicating that more Mg^{2+} will dissolve in basic solutions. This occurs because the hydroxide ion (OH^-), which is the primary form of Mg^{2+} in water, is more stable in basic solutions (Nishiki et al., 2023). As depicted in Figure 20d, pH decreased from 9.5 to 7.1 with CO_2, then increased slightly to 7.5. This increased Mg^{2+} concentration.

Aluminum concentration showed a declining behavior (Figure 20b). The solubility of aluminum hydroxide decreases with increasing temperature and ionic strength (Feng et al., 2008). The system's temperature was increased from 25 ºC to 95 ºC, and the lack of kaolinite in the system caused a decrease in aluminum concentration.

The solubility of calcium carbonate ($CaCO_3$) in water increases as the pH decreases, indicating that more $CaCO_3$ will dissolve in acidic solutions (Hart et al., 2013). This occurs because the carbonate ion (CO_3^{2-}) is more stable in acidic environments. The solubility of calcium (Ca^{2+}) in water decreases as the temperature rises (Straub, 1932). In the experiment, the Ca^{2+} concentration increased significantly (Figure 20c). This is attributed to the increasing acidity of the brine (Figure 20d). Consequently, a decrease in the

calcite mineral content of the assemblage was expected by the end of the experiment. However, XRD results indicate an increased trend (Figure 20). This behavior is likely due to the sudden pressure drop in the system, which led to $CaCO_3$ precipitation.

Silica concentration decreased from 105 to 67 ppm (Figure 21a). Consequently, it is unaffected by the pH of water. The solubility of silica is influenced by temperature. Specifically, the solubility of silica increases with rising temperature (Krauskopf, 1956). This occurs because water molecules can more easily break apart silica molecules at higher temperatures. Additionally, the solubility of silica is affected by the presence of other ions in the water. For example, the presence of Ca^{2+} can reduce the solubility of silica. This happens because Ca^{2+} can form complexes with the silica molecules, making them less soluble in water (Szymanek et al., 2021). A significant increase in Ca^{2+} concentration probably decreased silica solubility.

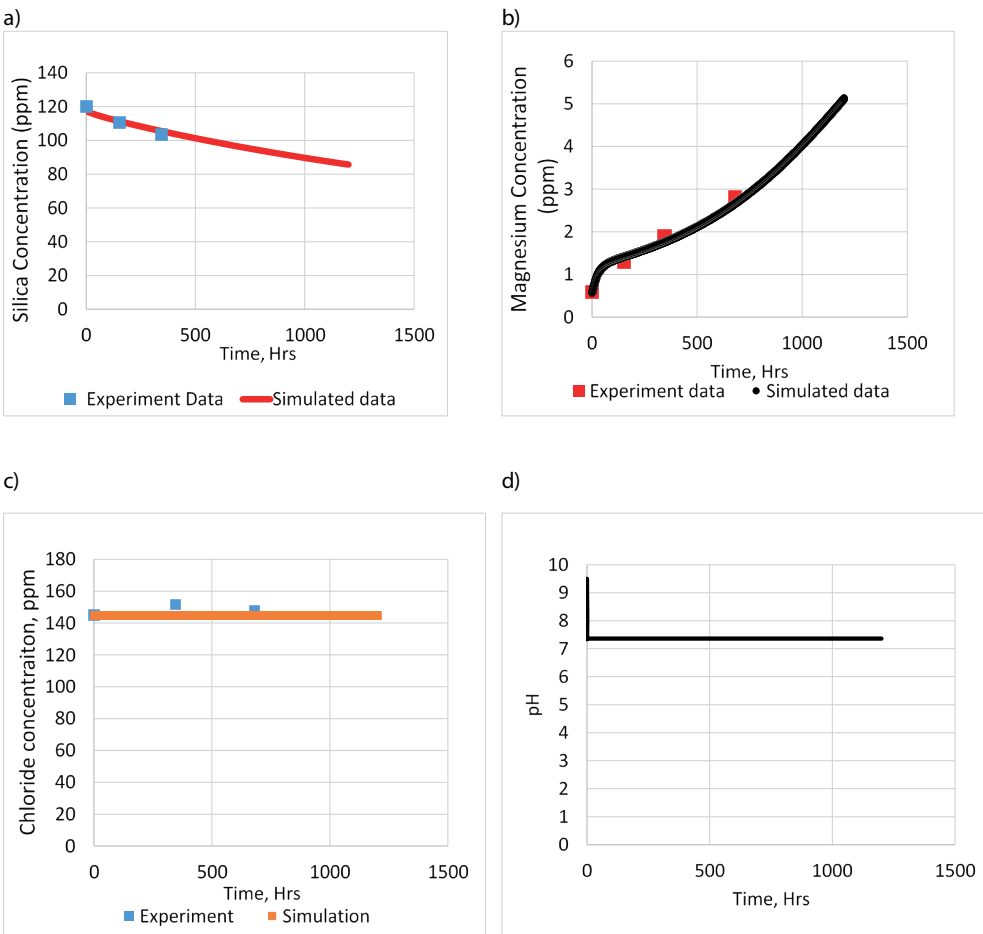

Figure 19. Experimental and simulation results for rock samples taken from 1900 m, a) SiO_2, b) Mg^{2+}, c) Cl^-, d) pH.
Şekil 19. 1900 m derinlikten alınan kaya örneklerine ait deney ve simülasyon sonuçları: a) SiO_2 b) Mg^{2+} c) Cl^- d) pH.

The solubility of Fe^{2+} in water is influenced by the pH of the solution. Iron dissolves more readily in acidic solutions compared to neutral or alkaline solutions. This increased solubility occurs because the iron atoms in acidic environments are more inclined to lose electrons, resulting in the formation of positively-charged ions (Fe^{2+} or Fe^{3+}). These ions are significantly more soluble in water than their neutral or negatively-charged counterparts (Liu & Millero, 2002). Lowering the pH from 9.5 to 7.1 raised iron solubility from 0.165 to 0.205 ppm (Figure 18b).

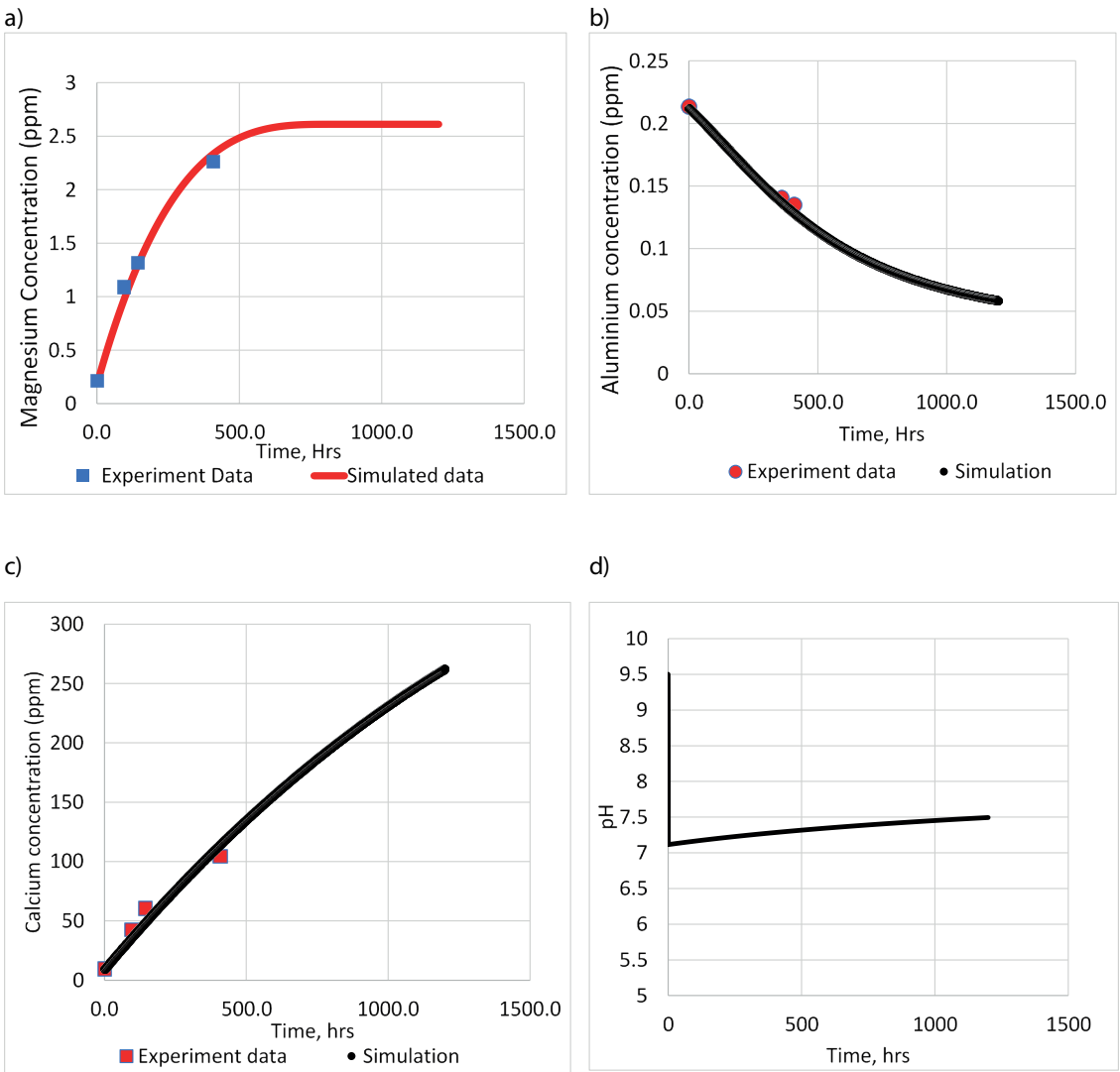

Figure 20. Experimental and simulation results for rock samples taken from 3000 m, a) magnesium, b) aluminum, c) Ca^{2+}, d) pH.

Şekil 20. 3000 m derinlikten alınan kaya örneklerine ait deney ve simülasyon sonuçları: a) magnesium b) aluminum c) Ca^{2+} d) pH.

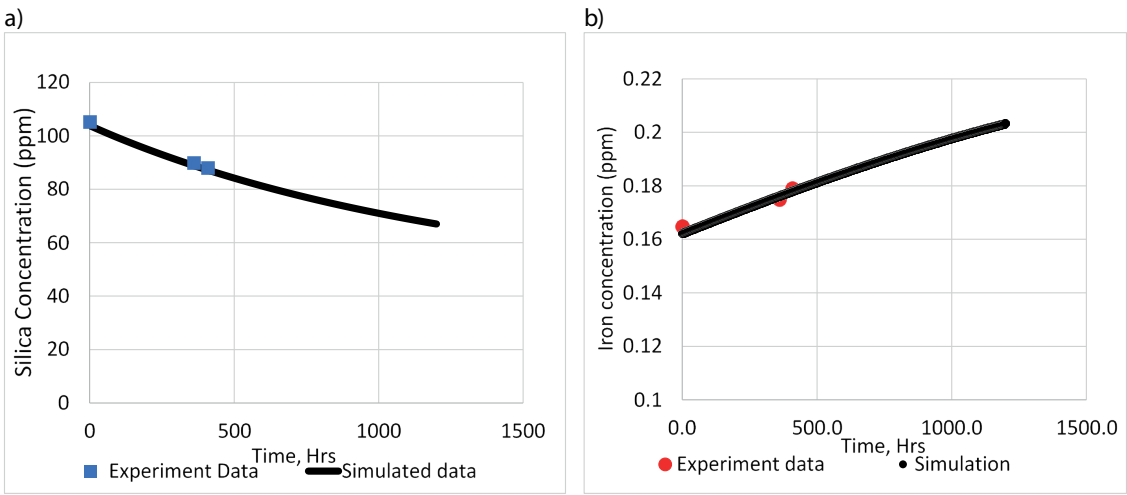

Figure 21. Experimental and simulation results for rock samples taken from 3000 m, a) silica, b) iron.
Şekil 21. 3000 m derinlikten alınan kaya örneklerine ait deney ve simülasyon sonuçları:a) silika b) demir

XRD results showed that rock samples involved specific alterations, such as siderite, magnesite, muscovite, kaolinite, dolomite, quartz, biotite, and feldspar (albite).

In the CO_2-saturated geofluid-rock interaction for the first mineral assemblage (1900 m), quartz, magnesite, dolomite, and siderite minerals exhibited a dissolution trend, while feldspar, kaolinite, and biotite demonstrated precipitation behavior. In the batch experiment with the second mineral assemblage (3000 m), calcite displayed precipitation behavior. The increasing acidity of the fluid favors calcite dissolution, as confirmed by Figure 20c, which indicates an increase in Ca^{2+} concentration. The rise in calcite content is likely associated with the experimental procedure; as the interaction is completed, the system is discharged to collect minerals for rock analysis following the experiment. During the discharge process, CO_2 is released, leading to calcite precipitation. Quartz and muscovite had dissolution trends. The pH of the solution decreased from 9.5 to 7.2 due to CO_2 dissolution in the brine. The decreasing pH caused a decline in silica in both batch experiments because solubility changes rapidly when pH exceeds 9.

In the studied batch experiments, the mineral assemblage remained the same while the abundance of the minerals changed. The study showed that the presence of cations such as Ca^{2+}, Al^{3+}, and Fe^{2+} promoted the precipitation of CO_2 as carbonates. The results of the batch experiments matched those of the PHREEQC results. The parameters adjusted for these matches were activation energy and kinetic reaction rates of the minerals. The tuning values of the parameters were in accord with USGS data for quartz, muscovite, pyrite, magnesite, siderite, and calcite. Discrepancies were observed for albite, kaolinite, and dolomite.

In the fluid-rock interaction experiments, the primary CO_2 trapping mechanism was identified as solubility trapping rather than mineralization. The results of solubility trapping can be found in Aydin and Akin (2023). CO_2 was measured using a gas flowmeter and alkalinity tests. The maximum gas content was determined to be 0.45% by weight under the experimental conditions. Siderite, magnesite, and calcite are the main minerals associated with CO_2 mineralization. As the $CaCO_3$ content of minerals was analyzed, 8.87 g of CO_2 was mineralized. Meanwhile, 40.5 g of CO_2 was dissolved in the geothermal brine.

Solubility trapping, although beneficial in the short- to medium-term due to its quick kinetics and high capacity under reservoir conditions, is essentially reversible. Pressure drops can cause CO_2 to degas, posing potential risks for remobilization and even leakage over time. Reinjection of waste brine is an industrial practice used to maintain the sustainability of geothermal production and reservoir pressure. Continuous re-injection can help mitigate long-term reservoir pressure declines. There are also specialized techniques for gas leakage monitoring, such as distributed temperature sensing (DTS), which utilizes fiber optics in the wellbore to detect gas leaks (Merey & Aydin, 2025), and remote sensing technologies like InSAR for monitoring ground subsidence and tilting during gas injection. Akın et al. (2025) observed soil CO_2 fluxes surrounding the faults in Kızıldere field before and after the demo-pilot gas injection at the nearby well. No significant variations were detected in shallow groundwater composition or soil CO_2 fluxes throughout the different phases of the injection.

It is important to note that the batch experiments were conducted under relatively lower pressure and temperature conditions compared to in situ conditions due to laboratory limitations. As a result, the kinetic rates and mineral stability observed in this study may differ from those under actual reservoir conditions, where elevated temperature and pressure significantly influence geochemical processes. While the findings provide valuable insights into water-rock interaction trends, they should be interpreted as indicative rather than fully representative of in situ behavior. Future studies will aim to incorporate high-pressure and high-temperature experiments to simulate reservoir conditions more accurately.

Although core samples were taken from the Kızıldere geothermal reservoir, the geothermal brine for the batch experiments was sourced from the Alaşehir field. This choice was mainly due to operational convenience, as the experimental setup was located in Alaşehir, allowing easy access to fresh geothermal brine from a nearby injection well. Additionally, previous hydrochemical analyses indicate that the geothermal fluids of Kızıldere and Alaşehir have similar Na-HCO_3-type water chemistry (Haklıdır & Sengun, 2020). Thus, using Alaşehir brine was appropriate for simulating water-rock interactions under representative conditions. However, we recognize that using brine directly from Kızıldere would have provided a more site-specific understanding of fluid-rock interactions. This limitation is acknowledged, and future studies will include parallel experiments with brine from the Kızıldere reservoir to enable more detailed comparisons.

CONCLUSION

This study offers a comprehensive understanding of the geochemical changes and mineral reaction kinetics during CO_2 sequestration in Paleozoic metamorphic rocks,

utilizing a detailed experimental and simulation approach.

Our investigations underscore the efficiency and stability of CO_2 sequestration through solubility trapping mechanisms compared to mineral trapping under the studied conditions. Importantly, the high cation concentrations present in the metamorphic rocks of the Kızıldere geothermal reservoir positively contribute to the CO_2 trapping potential. These geochemical insights are critical for optimizing CO_2 sequestration strategies in similar geological settings worldwide.

Crucially, batch experiments conducted at 95 °C and 10 bar revealed that a substantial portion of CO_2 (0.45% by weight, corresponding to 40.5 grams in 9 liters of brine) was trapped as dissolved gas, highlighting the dominance of solubility trapping over mineral trapping, where only 8.87 grams of CO_2 were mineralized. This predominance of solubility trapping emphasizes the importance of solution geochemistry in optimizing CO_2 sequestration strategies.

The experiments also indicated potential challenges associated with SiO_2 precipitation, notably as the pH decreased from 9.5 to 7.2, conditions were unfavorable for SiO_2 dissolution. Therefore, it is critical to maintain the injection temperature above the silica saturation temperature to mitigate SiO_2 precipitation.

Furthermore, a comparison between various rock depths indicates that the reservoir rock at a depth of 3000 m may be more conducive to CO_2 injection. This phenomenon can be attributed to the enhanced injectivity potential resulting from the interactions between CO_2-saturated brine and rock at this specific depth.

Future research should aim to broaden the experimental parameters to encompass different pressures and temperatures; thereby, more accurately simulating the natural conditions of geothermal reservoirs. Moreover, extended reaction studies are essential to comprehend the sustainability and long-term ramifications of mineral alterations on the efficacy of CO_2 trapping. Such insights will be critical in refining our understanding of geological CO_2 storage mechanisms and improving the reliability of these methods in mitigating atmospheric CO_2 levels; hence, contributing to global climate change mitigation strategies.

Nomenclature

k_1 is the specific rate constant in mol/mol^2/sec at 25 ºC,

k_2 is the specific rate constant at a specified temperature in Kelvin (T_K),

R is the gas constant, 8.3145 J/mole,

E is the activation energy for each mineral, J/mole,

SR is the saturation ratio (ion activity/equilibrium constant) with transition-state theory,

m_0 is the initial moles of the kinetic reactant,

A_0 is the initial surface area of mineral in meter^2,

V is the solution volume in contact with A_0 in liters; concentration is in mg/L.

REFERENCES

Akın, T., & Kargı, H. (2019). Modeling the geochemical evolution of fluids in geothermal wells and its implication for sustainable energy production. *Geothermics*, 77, 115-129.

Akın, T., Erol, S., Tokel, A.B., Sevindik, D.B., & Akın, S. (2025). Monitoring CO_2 injection in the Kızıldere geothermal field. *International Journal of Greenhouse Gas Control*, *146*, 104413.

Aksu, B. (2019). *Structural controls on Kızıldere geothermal field, Denizli-Turkey*[Master's thesis, Middle East Technical University (Turkey)].

Alçiçek, H. (2007). Denizli Havzası (Denizli-Buldan Bölgesi, GB Türkiye) Neojen Çökellerinin Sedimantolojik İncelemesi [Sedimentological Investigation of Neogene Deposits in Denizli Basin (Denizli-Buldan Region, SW Turkey)] (PhD thesis). Ankara University, Geological Engineering Department, p. 308.

Alçiçek, H., Varol, B. & Özkul, M. (2007). Sedimentary facies, depositional environments and palaeogeographic evolution of the Neogene Denizli Basin, SW Anatolia, Turkey. *Sedimentary Geology,* 202(4), 596–637. doi:10.1016/j.sedgeo.2007.06.002

Alt, J.C., Shanks III, W.C., Crispini, L., Gaggero, L., Schwarzenbach, E.M., Früh-Green, G.L., & Bernasconi, S.M. (2012). Uptake of carbon and sulfur during seafloor serpentinization and the effects of subduction metamorphism in Ligurian peridotites. *Chemical Geology*, *322*, 268-277.

Aydin, H., & Akin, S. (2023). CO2 Dissolution in the reservoir brine: An experimental and simulation-based approach. *Geothermics*, *113*, 102774.

Battles, D.A., & Barton, M.D. (1995). Arc-related sodic hydrothermal alteration in the western United States. *Geology*, *23*(10), 913-916.

Bénézeth, P., Dandurand, J.L., & Harrichoury, J.C. (2009). Solubility product of siderite (FeCO3) as a function of temperature (25–250 C). *Chemical Geology*, *265*(1-2), 3-12.

Berndsen, M., Erol, S., Akın, T., Akın, S., Nardini, I., Immenhauser, A., & Nehler, M. (2024). Experimental study and kinetic modeling of high temperature and pressure CO_2 mineralization. *International Journal of Greenhouse Gas Control*, *132*, 104044.

BingLin, Z., LiQiang, Y., SuoYing, H., Yue, L., WenLong, L., RongXin, Z.,... & ShengGuang, L. (2014). Hydrothermal alteration in the Jiaojia gold deposit, Jiaodong, China. *Acta Petrologica Sinica*, *30*(9), 2533-2545.

Blanc, Ph., Lassin, A., Piantone, P., Azaroual, M., Jacquemet, N., Fabbri, A. and Gaucher, E.C.: Thermoddem: A geochemical database focused on low temperature water/rock interactions and waste materials, *Applied Geochemistry*, 27, 10, (2012), 2107-2116.

Boray A. (1982). Selimiye-Beşparmak yöresindeki (Muğla) Menderes Masifi kayalarının stratigrafisi: tartışma ve Yanıt. *Türkiye Jeoloji Kurumu Bülteni*, 25, 161–162.

Bozkaya, Ö., Bozkaya, G., Akın, T., & Atan, H. (2024). Mineralogical and geochemical characteristics of alteration minerals related to fossil geothermal activities in the Kızıldere geothermal field, Western Turkey. *Geochemistry*, *84*(4), 126082.

Bozkurt, E. (2000). Timing of Extension on the Büyük Menderes Graben, Western Turkey, and Its Tectonic Implications. Geological Society, London, Special Publications, 173(1), 385–403. doi:10.1144/gsl.sp.2000.173.01.18

Bozkurt, E., & Oberhänsli, R. (2001). Menderes Massif (Western Turkey): structural, metamorphic and magmatic evolution - a synthesis. *International Journal of Earth Sciences,* 89(4), 679–708. doi:10.1007/s005310000173.

Bray, A. W., Oelkers, E.H., Bonneville, S., Wolff-Boenisch, D., Potts, N.J., Fones, G., & Benning, L. G. (2015). The effect of pH, grain size, and organic ligands on biotite weathering rates. *Geochimica et Cosmochimica Acta*, *164*, 127-145.

Brimhall, G.H., & Ghiorso, M.S. (1983). Origin and ore-forming consequences of the advanced argillic alteration process in hypogene environments by magmatic gas contamination of meteoric fluids. *Economic Geology*, *78*(1), 73-90.

Delerce, S., Marieni, C. & Oelkers, E.H. (2023). Carbonate geochemistry and its role in geologic carbon storage. *Surface Process, Transportation, and Storage*, 423-477.

Di Tommaso, I. & Rubinstein, N. (2007). Hydrothermal alteration mapping using ASTER data in the

Infiernillo porphyry deposit, Argentina. *Ore Geology Reviews*, *32*(1-2), 275-290.

Erol S, Akın T, Başer A, Saraçoğlu Ö, Akın S (2022a). Geofluid-CO_2 injection impact in a geothermal reservoir: Evaluation with 3-D reactive transport modeling. *Geothermics* 98: 102271. https://doi.org/10.1016/j.geothermics.2021.102271.

Erten, A., Eroglu, M., Avci, İ., Karan, T., & Çoban, A.E. (2021). Prevention of the Antimony Compounds at the Geothermal Power Plants with HYDRODIS® GE Products. Bilge International Journal of Science and *Technology Research*, 5(2), 146-156.

Feng, X., Zhang, B., & Chery, L. (2008). Effects of low temperature on aluminum (III) hydrolysis: Theoretical and experimental studies. *Journal of Environmental Sciences,* 20(8), 907-914.

Gürer, Ö.F., Sarıca-Filoreau, N., Özburan, M., Sangu, E. & Doğan, B. (2009). Progressive development of the Büyük Menderes Graben based on new data, western Turkey. *Geological Magazine,* 146(5), 652–673. doi:10.1017/s0016756809006359

Haklıdır, F.S.T., & Şengün, R. (2020). Hydrogeochemical similarities and differences between high temperature geothermal systems with similar geologic settings in the Büyük Menderes and Gediz Grabens of Turkey. *Geothermics*, *83*, 101717.

Haklıdır, F.S.T., Şengün, R. & Aydın, H. (2021). Characterization and Comparison of geothermal fluids geochemistry within the Kızıldere Geothermal Field in Turkey: New findings with power capacity expanding studies. *Geothermics*, 94, 102110.

Hart, P.W., Colson, G.W., & Burris, J. (2013). Application of carbon dioxide to reduce water-side lime scale in heat exchangers. *Pulp Pap. Canada*, *114*(1), 21-24.

Hellevang, H., Pham, V.T., & Aagaard, P. (2013). Kinetic modelling of CO_2–water–rock interactions. *International Journal of Greenhouse Gas Control,* 15, 3-15.

Hikov, A. (2004). Geochemistry of strontium in advanced argillic alteration systems–a possible guide to exploration. *Geology*, 16-17.

Kampman, N., Bickle, M., Wigley, M. & Dubacq, B. (2014). Fluid flow and CO2–fluid–mineral interactions during CO2-storage in sedimentary basins. *Chemical Geology*, *369*, 22-50.

Karamanderesi, İ.H., Helvaci C. (2003). Geology and hydrothermal alteration of the Aydın–Salavatlı geothermal field, western Anatolia, Turkey. T*urk J Earth Sci* 12:175–198.

Kaymakci, N. (2006). Kinematic development and paleostress analysis of the Denizli Basin (Western Turkey): implications of spatial variation of relative paleostress magnitudes and orientations. *Journal of Asian Earth Sciences*, 27(2), 207–222. doi:10.1016/j.jseaes.2005.03.003

Koçyiğit, A. (2015). An overview on the main stratigraphic and structural features of a geothermal area: the case of Nazilli-Buharkent section of the Büyük Menderes Graben, SW Turkey. *Geodinamica Acta*, 27(2-3), 85–109. do:10.1080/09853111.2014.957501

Krauskopf, K.B. (1956). Dissolution and precipitation of silica at low temperatures. *Geochimica et Cosmochimica Acta*, *10*(1-2), 1-26.

Krupp, R.E. (1988). Solubility of stibnite in hydrogen sulfide solutions, speciation, and equilibrium constants, from 25 to 350°C. Geochimica et *Cosmochimica Acta*, 52(12), 3005–3015. https://doi.org/10.1016/0016-7037(88)90164-0

Kumar, G.S., & Ghassemi, A. (2005). Numerical modeling of non-isothermal quartz dissolution/precipitation in a coupled fracture–matrix system. *Geothermic*, *34*(4), 411-439.

Liu, B., Xu, J., Li, Z., Malekian, R. & Xu, Z. (2018). Modeling of CO_2 transport and pressure buildup in reservoirs during CO_2 storage in saline

aquifers: a case in Dongying Depression in China. *Environmental Earth Sciences*, *77*, 1-14.

Liu, F., Lu, P., Griffith, C., Hedges, S.W., Soong, Y., Hellevang, H. & Zhu, C. (2012). CO_2–brine–caprock interaction: Reactivity experiments on Eau Claire shale and a review of relevant literature. *International Journal of Greenhouse Gas Control*, *7*, 153-167.

Malmström, M. & Banwart, S. (1997). Biotite dissolution at 25C: The pH dependence of dissolution rate and stoichiometry. *Geochimica et Cosmochimica Acta*, *61*(14), 2779-2799.

Mendoza, E.Y.M., Santos, A.S., López, E.V., Drozd, V., Durygin, A., Chen, J. & Saxena, S.K. (2019). Iron oxides as efficient sorbents for CO_2 capture. *Journal of Materials Research* and Technology, 8(3), 2944-2956.

Merey, Ş. & Aydın, H. (2025). Simulating hydrogen adsorption-driven thermal variations for improved well integrity monitoring in underground hydrogen storage. *International Journal of Hydrogen Energy*.

Meunier, A. & Velde, B. (1976). Mineral reactions at grain contacts in early stages of granite weathering. *Clay Minerals*, *11*(3), 235-240.

Musa, T.N. & Hamoshi, E.A. (2012). The effect of magnetic field on the solubility of NaCl and $CaCl_2$. $2H_2O$ at different temperature and pH values. *Basrah Journal of Agricultural Sciences*, *25*(1), 19-26.

Nishiki, Y., Cama, J., Otake, T., Kikuchi, R., Shimbashi, M. & Sato, T. (2023). Formation of magnesium silicate hydrate (MSH) at pH 10 and 50° C in open-flow systems. *Applied Geochemistry*, *148*, 105544.

Olsen, N.J., Mountain, B.W. & Seward, T.M. (2012). Experimental study of stibnite solubility in aqueous sulfide solutions from 25 to 90°C. New Zealand Geothermal Workshop, 19(November).

Palandri, J.L., & Kharaka, Y.K. (2004). A compilation of rate parameters of water-mineral interaction kinetics for application to geochemical modeling. Geological Survey Menlo Park CA.

Parkhurst DL, Appelo CAJ (2013). Description of input and examples for PHREEQC version 3 a computer program for speciation, batch-reaction, one-dimensional transport, and inverse geochemical calculations. U.S. Geological Survey Techniques and Methods. Amsterdam, Netherlands. https://pubs.usgs.gov/tm/06/a43/.

Parkhust, David L. 2005. PHREEQC, Modeling of Geochemical Reactions, Calculation of pH, Redox Potential. PHREEQCI, Windows Interactive Version of PHREEQC. PHRQCGRF, code to create graphs from the data generated by PHREEQC. U.S. Geological Survey.

Parry, W.T., Jasumback, M. & Wilson, P.N. (2002). Clay mineralogy of phyllic and intermediate argillic alteration at Bingham, Utah. *Economic Geology*, *97*(2), 221-239.

Pearce, J.K., Kirste, D.M., Dawson, G.K., Farquhar, S.M., Biddle, D., Golding, S.D., & Rudolph, V. (2015). SO_2 impurity impacts on experimental and simulated CO_2–water–reservoir rock reactions at carbon storage conditions. *Chemical Geology*, *399*, 65-86.

Peng, D.Y., & Robinson, D.B. (1976). A new two-constant equation of state. *Industrial & Engineering Chemistry Fundamentals,* 15(1), 59-64.

Phillipson, A. (1918). Kleinasien, Handbuch der Regionalen Geologie, edited by G. Steinmann and O. Wilckens, 5, Heidelberg.

Rao, F., Ramirez-Acosta, F.J., Sanchez-Leija, R.J., Song, S. & Lopez-Valdivieso, A. (2011). Stability of kaolinite dispersions in the presence of sodium and aluminum ions. *Applied Clay Science*, *51*(1-2), 38-42.

Ratouis TMP, Snæbjörnsdóttir SO, Sigfússon B, Gunnarsson I, Voigt MJ et al. (2021). Reactive transport model of CO_2 and H_2S mineral sequestration at the CarbFix2 reinjection site,

Hellisheiði Geothermal Power Plant, SW-Iceland. In: World Geothermal Congress (WGC) October 24-27, Reykjavik, Iceland.

Ratouis TMP, Snæbjörnsdóttir SÓ, Voigt MJ, Sigfússon B, Gunnarsson G et al. (2022). Carbfix 2: A transport model of long-term CO_2 and H_2S injection into basaltic rocks at Hellisheidi, SW-Iceland. International Journal of Greenhouse Gas Control 114: 103586. https://doi.org/10.1016/j.ijggc.2022.103586.

Samadi, R., Torabi, G., Kawabata, H. & Miller, N.R. (2021). Biotite as a petrogenetic discriminator: chemical insights from igneous, meta-igneous and meta-sedimentary rocks in Iran. *Lithos*, *386*, 106016.

Seki, Y. (1973). Metamorphic facies of propylitic alteration. *J. Geol. Soc. Japan*, *79*, 771-780.

Şengör, A.M.C., & Yilmaz, Y. (1981). Tethyan evolution of Turkey: A plate tectonic approach. *Tectonophysics*, 75(3-4), 181–241. doi:10.1016/0040- 1951(81)90275-4

Sengör, A.M.C., Satir, M. & Akkök, R. (1984). Timing of tectonic events in the Menderes Massif, western Turkey: Implications for tectonic evolution and evidence for pan-African basement in Turkey. *Tectonics*, 3(7), 693–707. doi:10.1029/tc003i007p00693.

Senturk, E., Aydin, H., & Tuzen, M.K. (2020, February). Injection Rehabilitation at Kızıldere Geothermal Field: Use of Flow Rate Weighted Average Production Wellhead Pressure for Reservoir Management. In *45th Workshop on Geothermal Reservoir Engineering, Stanford University; Stanford, California, United States*.

Shukla, R., Ranjith, P., Haque, A., & Choi, X. (2010). A review of studies on CO_2 sequestration and caprock integrity. Fuel, 89(10), 2651-2664.

Silva, C.A., Liu, X., & Millero, F.J. (2002). Solubility of siderite ($FeCO_3$) in NaCl solutions. *Journal of solution chemistry*, *31*(2), 97-108.

Şimşek, Ş. (1984). Denizli-Kızıldere-Tekkehamam-Tosunlar-Buldan-Yenice alanının jeolojisi ve jeotermal enerji olanakları. Mineral Res. Expl. Direct. Turkey (MTA), Scientific Report No: 7846, p. 85. Ankara, Turkey (in Turkish).

Steel, L., Mackay, E. & Maroto-Valer, M.M. (2018). Experimental investigation of CO_2-brine-calcite interactions under reservoir conditions. *Fuel Processing Technology*, *169*, 122-131.

Straub, F.G. (1932). Solubility of calcium sulfate and calcium carbonate at temperatures between 182 °C and 316 °C. *Industrial & Engineering Chemistry*, *24*(8), 914-917.

Sun, S. (1990). Denizli-Uşak Arasının Jeolojisi ve Linyit Olanakları [Geology of the area between Denizli and Uşak and lignite occurrences] (Report No. 9985) General Directorate of Mineral Research and Exploration (MTA) [in Turkish, unpublished].

Szymanek, K., Charmas, R. & Piasecki, W. (2021). Investigations of mechanism of Ca^{2+} adsorption on silica and alumina based on Ca-ISE monitoring, potentiometric titration, electrokinetic measurements and surface complexation modeling. *Adsorption*, *27*(1), 105-115.

Teng, Y., Wang, P., Xie, H. & Zhu, J. (2022). Capillary trapping characteristics of CO_2 sequestration in fractured carbonate rock and sandstone using MRI. *Journal of Natural Gas Science and Engineering*, *108*, 104809.

Waldmann, S., Busch, A., Van Ojik, K, & Gaupp, R. (2014). Importance of mineral surface areas in Rotliegend sandstones for modeling CO_2–water–rock interactions. *Chemical Geology*, *378*, 89-109.

Wallace, C.J. & Maher, K.C. (2019). Phyllic alteration and the implications of fluid composition at the Copper Flat hydrothermal System, New Mexico, USA. *Ore Geology Reviews*, *104*, 273-293.

Wang, K., Xu, T., Wang, F. & Tian, H. (2016). Experimental study of CO_2–brine–rock interaction during CO_2 sequestration in deep coal seams. *International Journal of Coal Geology*, *154*, 265-274.

White, A.F., & Brantley, S.L. (2003). The effect of time on the weathering of silicate minerals: why do weathering rates differ in the laboratory and field?. *Chemical Geology*, *202*(3-4), 479-506.

Witt, W.K. (1988). Evolution of high-temperature hydrothermal fluids associated with greisenization and feldspathic alteration of a tin-mineralized granite, northeast Queensland. *Economic Geology*, *83*(2), 310-334.

Zhang, D. & Song, J. (2014). Mechanisms for geological carbon sequestration. *Procedia IUTAm*, *10*, 319-327.